Radiation Measurements of Shockwaves in Synthetic Air and Pure Nitrogen

Alex B. Glenn*, Orin Varley†, Peter L. Collen ‡ and M. McGilvray§
Osney Thermofluids Institute, University of Oxford, United Kingdom

Absolute radiance measurements in synthetic air and pure nitrogen have been performed in the Oxford T6 Stalker Tunnel while operating in Aluminium Shock Tube mode. Spatially and spectrally resolved data have been attained for shock speeds from 5.7 to 8 km/s and post-shock pressures from ~10 to ~100 kPa. Two independent telecentric optical set ups acquire data from the UV/Vis (200 to 520 nm) and Vis/NIR (585 to 850 nm) regions. The data are presented in multiple formats. An example 2D spectral-spatial map of absolute radiance is provided. Equilibrium spectral radiance comparisons against CEA-NEQAIR demonstrate improved agreement since prior campaigns in both T6 and the Electric Arc Shock Tube at NASA Ames. Spatial radiance profiles demonstrate lower pressure conditions can improve the resolution of non-equilibrium relaxation. Finally, spectral profiles progressing through the relaxation region for a low pressure synthetic air test case are shown. The motivation of this paper is to provide reliable calibrated data that, in future work, can be used to extract thermochemical rates and upon which numerical codes and facility results can be benchmarked against.

I. Introduction

Thermochemical phenomena that occur during a planet entry mission, as a result of the high-temperature gas effects, have been studied since the 1960s. Dissociation, ionisation and radiation emission occur under such conditions, as species in excited energy states try to relax to a new equilibrium. Though these events have detrimental implications to entry vehicle design, the radiation emission provides a means to perform non-intrusive optical spectroscopy measurements. Due to the expense of real flight experiments, ground test facilities have traditionally been used to recreate these high-enthalpy flow environments. This allows clean radiation data, amongst other parameters, to be captured to inform computational models. Experiments are routinely run on a number of ground test facilities, such as the Electric Arc Shock Tube (EAST) at NASA Ames [1] and Inductively Coupled Plasma (ICP) Torch at CentraleSupélec [2], where it is common practice to match the test gas composition to the planet's atmosphere. Such experiments have also previously been performed in the Oxford T6 Stalker tunnel [3–5], capable of operating in two shock tube modes [6–8]. Chemical kinetic rates are extracted [9] and implemented into computational models to predict the shock layer radiation environment ahead of an entry vehicle. High-speed entries (>10 km/s for air) warrant consideration due to radiative heating and are dominated by atomic spectral features [10–12]. At lower speeds, reaction rates decrease and the non-equilibrium region can contribute a more significant portion of the total shock layer radiation. Also at these speeds, radiation is dominated more by molecular features, such as NO, N_2 and N_2^+ for Earth entry. This exercises different components of computational models, which have shown greater disagreement to both EAST and T6 shock tube facilities [6, 13] in synthetic air at these lower speeds. Reducing uncertainties of non-equilibrium radiation has been identified as one of planet entry gas dynamics' highest priorities for the last 20 years [14]. However, without good agreement between experimental and numerical equilibrium spectra, reliable studies of non-equilibrium relaxation reactions will be skewed by these discrepancies from the start. Improving the agreement of experiment and numerical predictions in the equilibrium region validates both radiation measurements and modelling against one another. Once this is achieved, then the additional complexity of chemical kinetics can be introduced, in the confidence that experiment and simulation reach the same end state. This paper provides a new dataset of synthetic air (20.9% O_2 / 79.1% N_2) and pure nitrogen conditions relevant to Low Earth Orbit (LEO) re-entry speeds. Upgrades including a new telecentric optical system and more thorough cleaning techniques have resulted in better agreement of equilibrium spectra to numerical predictions than has been demonstrated in previous campaigns in both T6 [6] and EAST [13].

*DPhil Candidate, Department of Engineering Science, Oxford Thermofluids Institute, University of Oxford
†High Speed Research Engineer, Department of Engineering Science, Oxford Thermofluids Institute, University of Oxford
‡Postdoctoral Researcher, Department of Engineering Science, Oxford Thermofluids Institute, University of Oxford
§Professor, Oxford Thermofluids Institute, Department of Engineering Science, University of Oxford

By using the simplified gas mixtures of synthetic air and pure nitrogen, a simplified study can be performed thanks to limiting the number of species and reaction mechanisms. Synthetic air simplifies the test mixture from ambient air by removing trace species such as CO_2, H_2O vapour, Argon, etc. The pure nitrogen provides a further simplified test gas that can be used for model development of nitrogen rich atmospheres. Reducing the number of reactants in turn reduces the number of possible collision partners and the complexity of energy exchange reactions. Similar experiments have previously been performed in EAST (Test Releases 62) [15, 16] and the ICP torch [17]. The data herein extends the available dataset of synthetic air and pure nitrogen benchmark conditions generated by EAST, focusing on lower speeds (5.8 to 8.0 km/s) more relevant to LEO trajectories and a range of post-shock pressures (∼10 to ∼100 kPa).

Brandis and Cruden [15] highlight that by removing oxygen from synthetic air studies, the 11 species and 21 chemical reactions to consider are simplified to only 5 species (N, N^+, N_2, N_2^+, e^-) and 4 reaction mechanisms, summarised as:

$$N_2 + M \longleftrightarrow N + N + M \tag{1}$$

$$N + e^- \longleftrightarrow N^+ + e^- + e^- \tag{2}$$

$$N + N \longleftrightarrow N_2^+ + e^- \tag{3}$$

$$N^+ + N_2 \longleftrightarrow N_2^+ + N \tag{4}$$

Each of the species has characteristic spectral features as a result of relaxation via photon emission between discrete energy levels, across all degrees of freedom. These transitions are well documented in the NIST Atomic Spectral Database [18] for a range of species across many spectral regions. Thus, atomic lines and molecular bands can be identified and used to extract number densities and energy distributions. How these evolve temporally provides information of rates of thermal and chemical interactions. The more spectral features that can be captured, the more detailed the understanding of the species present and the thermochemical environment. During an experiment however, only smaller spectral regions can be captured in a given camera exposure, due to a finite camera CCD size and thus a compromise must be struck between spectral range and resolution. Data presented herein from the recent T6 Aluminium Shock Tube campaign provides spectral profiles in the UV/Vis (varying from 200 to 520 nm) and the Vis/NIR (typically 585 to 850 nm). Additionally, data acquired from EAST is shown for comparisons, spanning a larger spectral range from the VUV to IR. This is made possible by containing their optical setups in ultra low vacuum chambers to avoid ambient absorption.

The motivation of this paper is to provide reliable calibrated absolute radiance data for "Earth relevant" gas mixtures, that future codes and facilities can be benchmarked against. By demonstrating here the improved agreement between equilibrium radiance measurements with simulations, it is believed the new T6 Aluminium Shock Tube dataset provides reliable relaxation profiles to tune reaction rates against. All radiation data was acquired using two newly designed and implemented telecentric optical setups. Future work will involve more detailed analysis of the data, characterisation of the optical set up (including spectral and spatial smear functions) and application of state of the art codes to see how they fare against this new dataset and test conditions.

A description of the T6 Aluminium Shock Tube experimental set up is given in Section II, followed by a summary of upgrades in Section III and a map of conditions achieved in the recent test campaign in Section IV. A few remarks on the data processing are made in Section V, mainly regarding shock deceleration and stray light removal. Equilibrium spectral profiles from the recent T6 AST campaign are compared against that from previous campaigns and EAST in Section VI. Non-equilibrium relaxation profiles in pure nitrogen test cases are compared, as well as the UV/Vis spectral profile evolution through a low pressure synthetic air test case in Section VII. Finally, a brief example of carbon contamination effects for a more severe low pressure test case is given in Section VIII.

II. Experimental Setup

New absolute radiance measurements have been performed in the Oxford T6 Stalker Tunnel while operating in Aluminium Shock Tube (AST) mode, which has been described in detail in previous works by Collen [3, 4, 8]. Thus, only a brief summary is provided herein. Figure 1 shows a cross-section view of the T6 facility in AST mode. A free-piston driver is used to polytropically compress a helium-argon mixture in the compression tube until rupture of the primary diaphragm, to generate a shock wave which then travels downstream. Prior to this rupture, the AST section has been filled with a test gas relevant for the planet entry test case of interest. The normal shock wave progresses through the test gas, compressing and accelerating the gas to travel downstream. An analogy is made to relate the flow between the normal shock and the contact surface (with the driver gas) in the shock tube, to the stagnation streamline from the bow shock to the boundary layer edge ahead of an entry vehicle. The shock tube is filled with equivalent composition and density to the desired planet atmosphere and altitude, and a driver condition selected to produce a normal shock travelling at the same speed as the vehicle for the chosen trajectory point. This enables recreation of thermochemical evolution through the entire test slug, equivalent to the vehicle shock layer stagnation line, including the non-equilibrium and relaxation processes. After primary diaphragm rupture, the continued piston motion acts to delay expansion wave generation and propagation, helping to postpone shock deceleration. The driver gas expanding out into the driven section cushions the piston to allow for a "soft" landing at the end of the compression tube. An optional secondary driver between the driver and AST can be filled with helium, through use of a secondary diaphragm, to reach faster shock speeds [19] . In cases when it is not needed, there is no secondary diaphragm and the secondary driver is filled with the test gas.

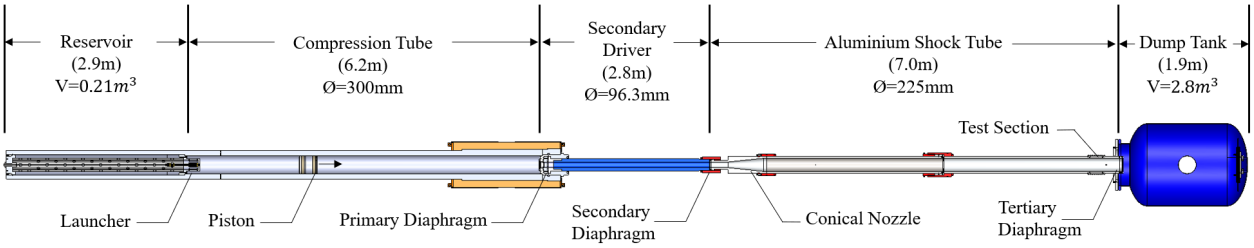

Fig. 1 Section view of T6 Stalker tunnel in Aluminium Shock Tube mode from above

Two major inconsistencies with the analogy between shock tube and entry vehicle stagnation line that have been highlighted in recent literature are: 1. Variations in shock speed within a shock tube experiment; 2. the presence of a growing boundary layer along the tunnel wall. The effect of the former has been well documented in works of Satchel et al. [20, 21] and Collen et al. [22], demonstrating shock speed variations directly lead to thermochemical gradients in the resulting test slug, which can be seen in radiance measurements. The latter has recently been documented in works of Clarke et al. [23]. The presence of a growing boundary layer around the circumference of the tube inner wall introduces differences in particle time of flight through a test slug, compared to a vehicle stagnation line. This is owed to extraction of particles from the test gas core flow as they are consumed by the boundary layer. Correcting for this particle time of flight has drastically reduced discrepancies between shock tube experimental data and simulations over a blunt body, originally thought owed to incorrect reaction rates. This correction is particularly important for gases or conditions with long relaxation times.

The design of the AST lends itself to low-speed shock layer radiation studies. The 225 mm diameter tube provides a large integration path-length for optically thin radiation, which increases signal-to-noise ratio. Reduced boundary layer effects results in less shock deceleration and therefore longer test gas slugs [24]. Considerable effort is devoted to minimising all leaks since inadequate sealing has the potential to invalidate all spectral data gathered. For the data presented here, ultimate pressures of less than 0.1 Pa were achieved, and leak rates measured from 0.7 to 1.3 mPa/s while at the ultimate pump down pressure.

Validation of test gas purity for the 100% nitrogen tests, and thus leak rate, was performed via test case T6s479. The UV/Vis spectrum for which, and the comparable synthetic air test case T6s476, is shown in Figure 2. This indicates that the leak rate was at an acceptable level to avoid contamination from ambient air and outgassing from the tunnel walls. This conclusion is based on the lack of signal from 200 to 280 nm, where nitric oxide, NO, radiates strongly for air test cases. This implies the absence of O_2 in the test gas, and thus an acceptable leak rate to confirm a pure nitrogen test gas. The signal that remains at these lower wavelengths is currently thought to be owed to a background continuum signal from bound-free and free-free electron interactions, such as Bremsstrahlung radiation [25], and/or remaining stray light. This is to be investigated in future works.

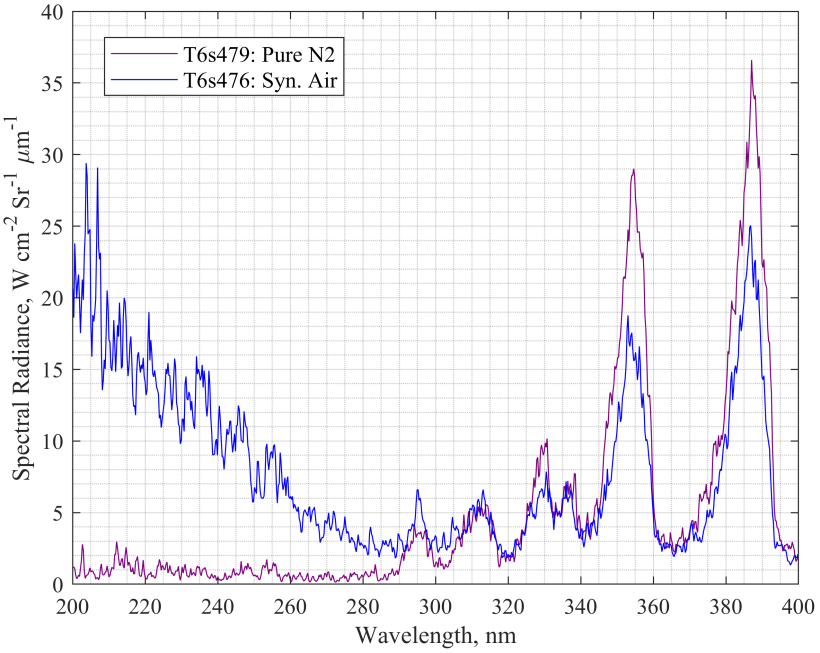

Fig. 2 UV/Vis spectra from pure nitrogen test case T6s479 (7.1 km/s shock speed at window, 73.2 Pa fill pressure and ~40.7 kPa post-shock pressure) and synthetic air test case T6s476(7.4 km/s, 71.6Pa fill, ~43 kPa post-shock pressur). Low signal below 280 nm in the pure nitrogen spectrum is indicative of lack of NO and thus acceptable leak rate to validate a pure nitrogen test case.

III. Upgrades

The intention of this paper is to present data in synthetic air and pure nitrogen from a recent campaign in the T6 AST and demonstrate improvements upon previous T6 and EAST datasets. To achieve these improvements, a number of optical and tunnel upgrades have been implemented from the previous T6 AST campaign setup, which has been comprehensively described by Collen [3]. This section gives a brief summary of the main upgrades, to provide context to the results shown in later sections. More detailed discussions will be provided in future papers.

A. Optical Setup

Primary analysis of the test gas is performed in the downstream section at the windows just before the dump tank, via a dual Optical Emission Spectroscopy (OES) setup. The UV/Vis optical set up is pictured in Figure 3. This is a newly designed and developed telecentric optical set up consisting of:

1) Two 200 mm by 25 mm periscope mirrors
2) 203.2 mm diameter focusing mirror
3) 200 mm diameter folding mirror
4) 76.2 mm diameter focusing mirror
5) 25.4 mm diameter cylindrical mirror

This is an upgrade from the original telescopic set up [6], designed with the intention to reduce spatial smear, reduce spatial smear function deviations along the tube axis and have a greater magnification to improve resolution of the relaxation regions. This is at the expense of field of view (FOV), typically ~85 mm as opposed to ~160 mm of the previous telescopic set up. The large 200 mm diameter mirrors were used to increase solid angle and thus signal-to-noise ratio, as well as future proof for alternative set ups that could incorporate the same initial focusing mirror, since FOV is limited by this. The Vis/NIR optical set up has the same mirrors, with different coatings and slightly different mirror positions due to spatial constraints. The UV/Vis mirrors used an $AlMgF_2$ coating, reported to have high reflectivity down to ~190 nm, while the Vis/NIR used protective silver coatings, with high reflectivities from ~400 nm upwards.

Fig. 3 Downstream end of the T6 Aluminium Shock Tube and UV/Vis telecentric optical setup.

Radiation emitted from the test gas escapes through two 200 mm long diametrically opposite windows along the tube axis, 9.3 m from the primary diaphragm. Both windows have their own telecentric optical path, as discussed, which map the radiation along a spectrometer slit. It is then spectrally separated by a diffraction grating while retaining its spatial profile along the tube axis. The wavelength-dispersed image finally falls on the camera sensor at the spectrometer outlet to capture the spatially and spectrally resolved image. An exposure time of 0.5μs was used for nearly all new test cases shown in the present work, to minimise smearing due to shock motion. Both sides used intensified Andor sCMOS cameras and Princeton Instruments Isoplane-320 spectrometers, with each pair tailored to their designated wavelength

region. Low resolution gratings of 150 G/mm were employed on the UV/Vis and Vis/NIR OES systems to provide access to a broad range of spectral features.

The raw images taken by the cameras provide data with signal in units of counts. In order to convert this to spectral radiance, calibrations were performed using a uniformly radiating integrating sphere to produce a full field calibration at wavelengths above 300 nm for both the Vis/NIR and UV/Vis optical paths. In addition, a Deuterium lamp is used to calibrate the UV/Vis wavelengths below 300 nm. Calibrations were performed before every test, following the methodology of Cruden [1].

To resolve the non-equilibrium relaxation accurately, the spatial resolution should be much smaller than the region with the thermochemical gradients to be resolved. Figure 4 compares the optical spatial smearing component of the new UV/Vis telecentric optical setup against that of the prior telescopic setup. Both functions have been acquired from ray tracing of the entire optical paths at 30 mm downstream from the window centre, typically where the shock is located during camera gating. This function is convolved with camera and shock motion smearing components as described by Cruden [1], to produce the final spatial smearing function. This will be characterised in more detail in future works.

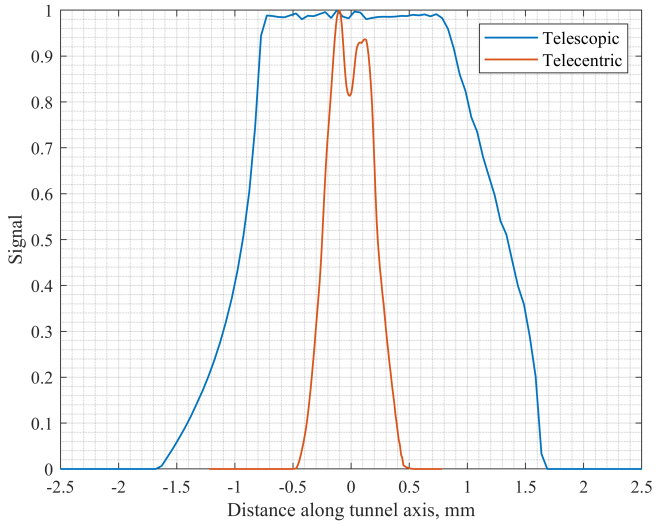

Fig. 4 Comparison of optical smear functions for the new telecentric and previous telescopic OES systems used in T6 AST campaigns. Ray traces in both cases are for the UV/Vis setups, 30 mm downstream from the window centre, where the shock is typically located during camera gating.

B. Slit Width

The new telecentric optical setups incorporate large 203.2mm focusing mirrors. These were used to: 1. allow for future optical system designs that may require a larger FOV (since that is limited by the size of the initial focusing mirror) and 2. produce a larger solid angle and thus more signal focused onto the spectrometer slits. Whether telecentric or telescopic, the spatial smearing can be reduced by decreasing the size of the aperture at a focusing lens, which in turn reduces the solid angle, and thus the signal with it. Similarly, the spectrometer slit width can be decreased to improve spectral resolution, again at the expense of signal. Improvements in spatial resolution from the new telecentric setup, even with the iris fully open, is demonstrated from the ray tracing smear functions, as shown in Figure 4. Since good resolution was attained without reducing the iris aperture, it was kept fully open for nearly all shots to provide camera pixels with as much signal as possible. Signal-to-noise ratio can be an issue at these lower speed conditions. This, in turn, allowed the spectrometer slit widths to be reduced from $\sim 100\mu m$ in the Vis/NIR and $\sim 170\mu m$ in the UV/Vis to $10\mu m$ for both (the lower limit for the Princeton Instruments Isoplane-320 spectrometers). Thus, both spectral resolution and spatial resolution are superior in the new telecentric optical setups.

It was noticed that when using a narrower slit width, the vertical offset in equilibrium data when compared against CEA-NEQAIR [26–28] was reduced, particularly at higher wavelengths. An offset between equilibrium spectral radiance and CEA-NEQAIR predictions had been an issue with previous datasets acquired in the T6 AST [6] and EAST

at similar conditions. An example of this is shown in Figure 5, comparing equilibrium spectral radiance for two recent similar test cases in synthetic air - both with fill pressures of 107 Pa and shock speeds at the window of 6.3 km/s and 6.55 km/s. T6s448 used wider slit widths, representative of those used in the previous T6 AST campaign. Exposure times were kept inversely proportional to slit widths, to keep raw signal levels on the cameras approximately the same for both cases. The wavelength region in the Vis/NIR is shifted, though the improved agreement with narrower slit width is most noticeable there. Some offset remains in the UV/Vis, and appears to increase with wavelength. This remaining offset at lower wavelengths is noticed to be more dominant for higher pressure test cases in both synthetic air and pure nitrogen from around 320 nm, as shown in Section VI.C. The removal of the vertical offset from a reduction in slit width is believed to be linked to removal of stray light in the spectrometer, though further investigation is needed. A slit width of $10\mu m$ was maintained for all the remaining shots in the recent T6 AST campaign.

C. Cleaning

For the new T6 AST data presented herein, cleaning of the internal shock tube walls from the secondary driver to the end of the AST section was performed before every test. This involves soaking a foam pipe cleaning "pig" with acetone and completing multiple passes up and down the tube until a fresh clean pig comes out still clean. This removes many of the carbon contaminants coated along the tunnel wall. The pig is fitted to have diameter slightly larger than the tunnel ID. Different material stiffnesses were trialled to optimise the process. After the acetone, a number of passes are completed with a pig soaked in isopropyl alcohol to remove any residue. Finally, the ends of the AST and secondary driver interfaces are cleaned manually with optical cloths soaked in the same cleaning solutions, with particular attention near the windows. This whole process is to remove solid carbon contaminants coated along the tunnel walls between shots. A number of trials using the IBSS GV10x 300W Downstream Asher on the final 2 m section of the AST were carried out, to see if any additional carbon could be removed. The details of this and further tests to investigate the remaining origins of hydrocarbon contaminants (i.e. leaks and outgassing) and their removal will be given in future papers. None of the data presented herein was attained after using the GV10x before the shot, only the cleaning pig process. In the previous campaign [6], cleaning was completed after just two passes of an acetone soaked pig, thus was not as thorough.

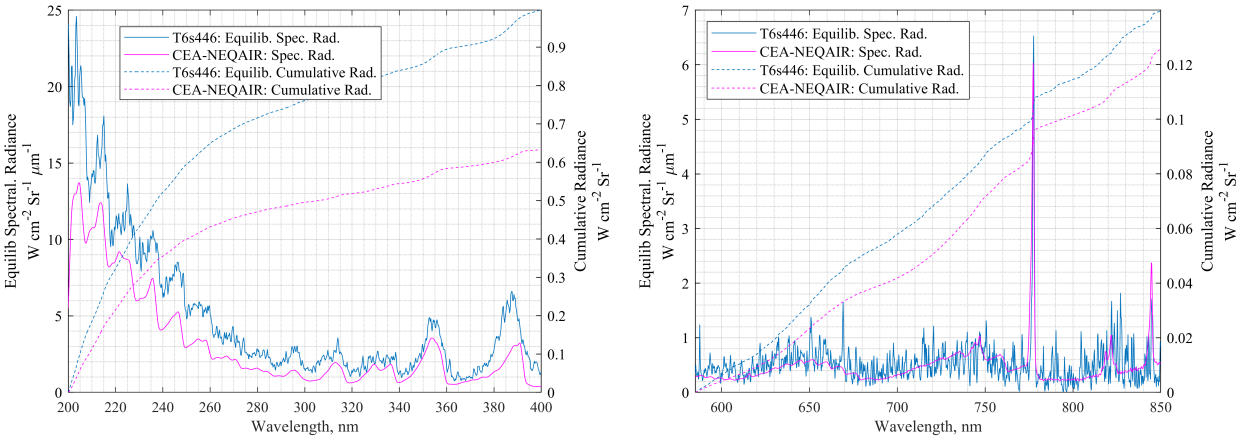

(a) T6s446 UV/Vis: 10μm slit

(b) T6s446 Vis/NIR: 10μm slit

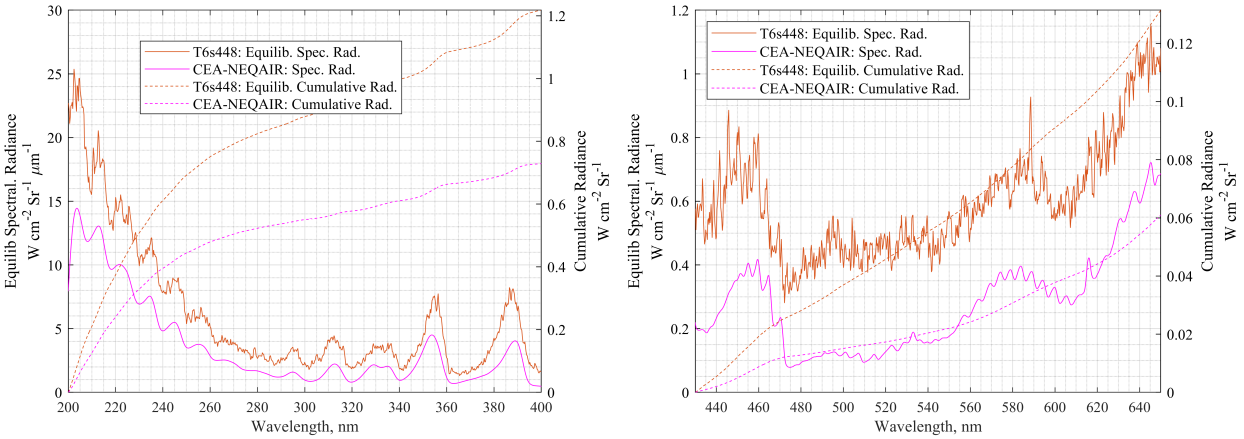

(c) T6s448 UV/Vis: 170μm slit

(d) T6s448 Vis/NIR: 100μm slit

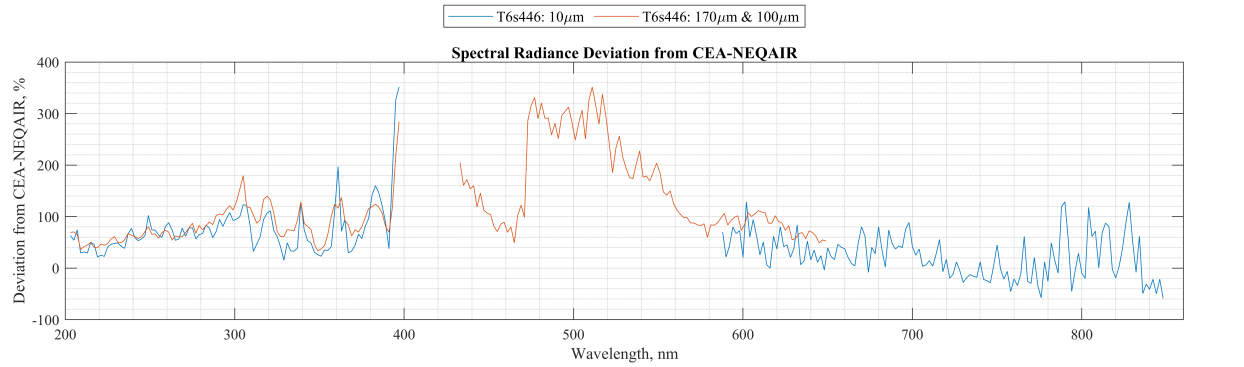

(e) Deviations from CEA-NEQAIR

Fig. 5 Equilibrium spectral radiance summary for T6s446 (6.3 km/s, 107 Pa fill) and T6s448 (6.55 km/s, 107 Pa fill) test cases against CEA-NEQAIR predictions. Both in synthetic air. The slit widths used are labelled in the sub figures.

IV. Conditions Tested

Figure 6 maps some of the test conditions achieved in synthetic air and pure nitrogen in the most recent T6 AST test campaign, ending in November 2023. Shock speeds range from 5.7 to 8.0 km/s, at a series of different targeted post-shock pressures - 100 kPa, 40kPa, 20 kPa and 10 kPa. The post-shock pressure is a direct indicator of the density of molecules/atoms and thus the frequency of their collisions, which determines the reaction rates and ultimately the size of the non-equilibrium relaxation region of the observed test slug. This gives the post-shock pressure more physical relevance to any rates extracted, and thus is the pressure plotted in the condition map to define the test condition. The pressures quoted are values averaged from shock timing stations near the shock front at the time of camera gating. In reality, the post-shock pressure varies through the test slug as a result of boundary layer effects, as discussed in the introduction. Simulations to study this more accurately will be run in future work, but the measured average stated should be a good indicator and agrees closely with CEA predictions.

The shock tube fill pressure and wavelength regions for test cases considered in the following sections of this paper are also given in Table 1. In theory, by varying the post-shock pressure, different fields of view (FOV) and spatial resolutions of a test slug's thermochemical relaxation, for a given shock speed, may be observed. At lower post-shock pressure, the non-equilibrium relaxation process exists over a larger spatial region, allowing it to be resolved with greater resolution, with the sacrifice of FOV and signal-to-noise ratio (since number densities of species actually radiating decreases and these conditions are close to being optically thin). Improving spatial resolution of the non-equilibrium region is important if aiming to extract rates of thermochemical processes, since the size of the non-equilibrium peak and subsequent relaxation should be larger than any of the spatial smearing components. Hence, the pressure is an additional parameter (to the optical, camera and gating components) that can be adjusted to improve the resolution of the post-shock relaxation processes.

An exposure time of 0.5μs was used for both intensified cameras in the remaining T6 AST test cases of the most recent campaign, to keep the Spatial Resolution Function (SRF) [1] approximately constant from shot to shot (since the shock speeds are fairly similar). This allows easier like-for-like comparison across the experimentally measured spatial radiance profiles. The SRF's for the new dataset will be characterised and documented in more detail in future work.

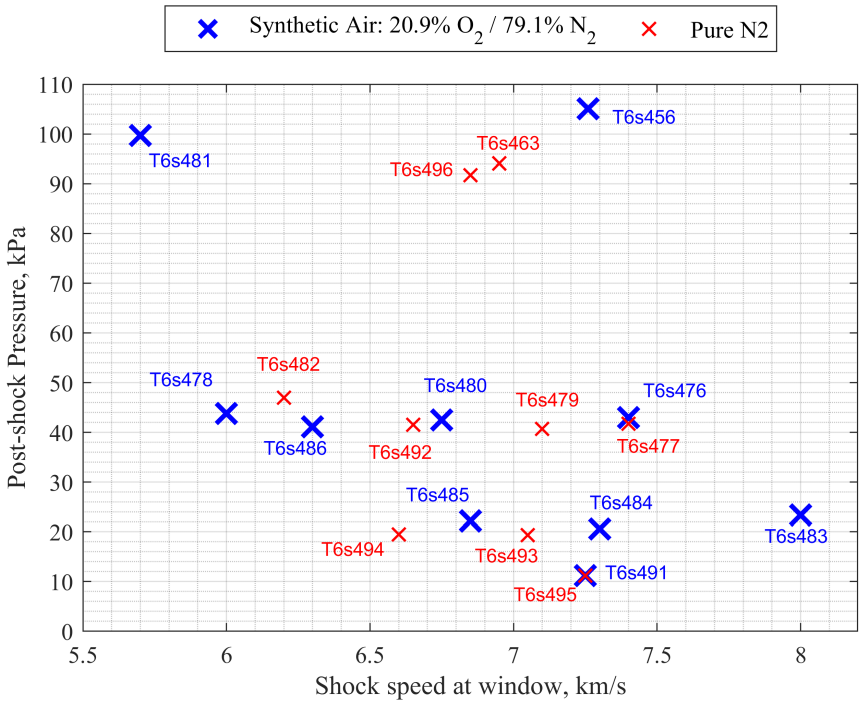

Fig. 6 Map of conditions achieved in synthetic air and pure nitrogen in recent T6 Aluminium Shock Tube test campaign

Table 1 Summary of synthetic air and pure nitrogen conditions obtained from recent T6 Aluminium Shock Tube test campaign, plus conditions from previous T6 AST and EAST campaigns. Post-shock pressure for the EAST test cases were calculated in CEA.

Shot No.	Gas	P_{fill} (Pa)	Us_{window} (km/s)	$P_{2,Approx}$ (kPa)	UV/Vis (nm)	Vis/NIR (nm)
T6s446	Syn. Air	107	6.3	49.5	200 - 400	585 - 850
T6s448	Syn. Air	107	6.55	53.0	200 - 400	430 - 650
T6s456	Syn. Air	175	7.26	105.1	200 - 400	585 - 850
T6s483	Syn. Air	33.0	8.0	23.4	200 - 400	585 - 850
T6s484	Syn. Air	33.3	7.3	20.6	200 - 400	585 - 850
T6s501	Syn. Air	33.4	7.23	20.0	335 - 393	585 - 850
T6s477	N_2	73.0	7.4	41.7	290 - 520	585 - 850
T6s482	N_2	107.5	6.2	47.0	290 - 520	585 - 850
T6s492	N_2	90.0	6.65	41.5	290 - 520	585 - 850
T6s494	N_2	40.5	6.6	19.5	290 - 520	585 - 850
T6s496	N_2	175	6.85	91.7	290 - 520	585 - 850
T6s207	Syn. Air	107	6.64	50.0	200 - 400	585 - 850
T6s245	N_2	201	6.84	105	290 - 520	600 - 840
EAST-59-42	Air	40	8.09	29.2	210 - 535	490 - 880
EAST-59-47	Air	94.7	6.81	48.6	210 - 535	490 - 880

Finally, as alluded to in the introduction, the variations in shock speed as it travels down the tube, directly impact the entropy gradients in the imaged test slug. With this in mind, the shock profiles for the test cases in Table 1 are plotted in Figure 7. The plotted points indicate the average shock speed between two consecutive shock timing stations. Straight lines between the points are used to aid readability, not to imply that shock speed is linear between the points. Error bars increase at the downstream end of the tube, near the window, due to closer spacing of shock timing stations.

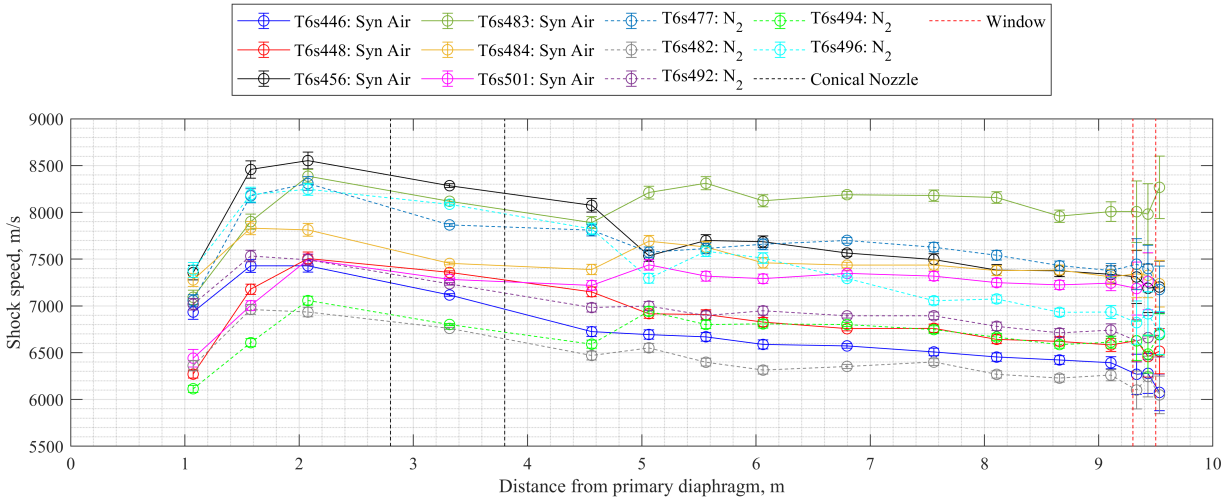

Fig. 7 Shock profiles for the synthetic air and pure nitrogen test cases from recent Aluminium Shock Tube campaign that are considered in the following sections of the paper

V. Data Processing

A. 2D Spectral Map

Figure 8 shows an example 2D calibrated absolute radiance map in the UV/Vis for T6s492 (6.65 km/s, 90 Pa fill pressure and ~41.5 kPa post-shock pressure). The signal is resolved spectrally along the x-axis and spatially along the y-axis, calibrated such that 0 mm is approximately where the shock front is expected to be. Positive direction is behind the shock front, with the shock travelling down the page. Thus, the flow is seen one dimensionally (in space) and signal is accumulated from radiation captured across the tube diameter from both core and boundary layer regions.

The horizontal lines indicate regions chosen to average radiance over, which when plotted against wavelength make spectral radiance profiles, as shown in the plot below the 2D map. The red horizontal lines average over the non-equilibrium region with peak radiance, where as the blue horizontal lines average over the region where relaxation appears to just finish, for this test case. This flat region would be considered the "equilibrium region". By averaging over a spatial region of constant radiance, the signal-to-noise ratio of the resulting spectral radiance profile is improved.

Integrating between the black vertical lines, and thus summing the radiance across the wavelengths, at each point in space results in a cumulative radiance plot against space. An example spatial radiance profile is plotted to the right of the 2D radiance map, calculated from the position of the black vertical lines shown. This integration can be made across any desired wavelength regions, allowing the radiance profile from individual spectral features to be extracted.

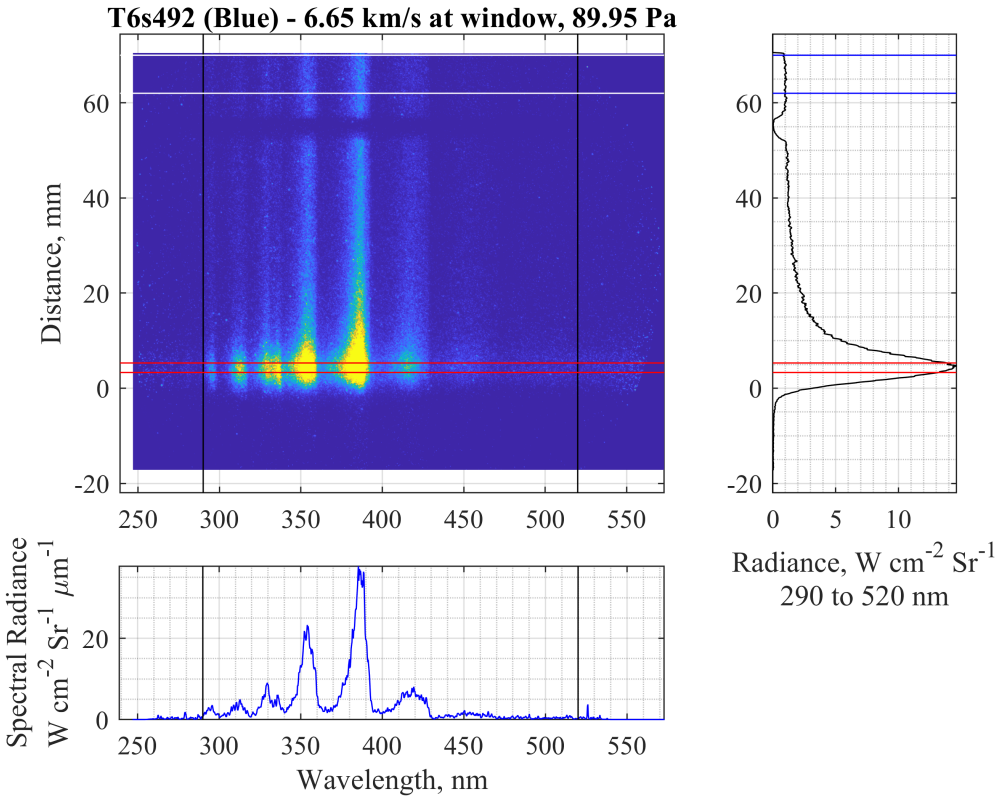

Fig. 8 T6s492 UV/Vis 2D map of spatially and spectrally resolved absolute radiance

Figure 9 re-plots the resulting spatial and spectral radiance profiles from the regions selected in Figure 8. The dip in signal from ~52 to ~58 mm is a consequence of light being blocked to enable an alternative stray light removal method. This is explained in more detail in the following section. Additionally, the equilibrium spectral radiance in Figure 9b is compared against a CEA-NEQAIR prediction. The non-equilibrium spectral radiance plot shows similar spectral features, though much more intense. The different ratios of peaks between spectral features indicate different species concentrations and energy state distributions, as is to be expected in the region where reactions are occurring and neither thermal nor chemical equilibrium have yet been attained.

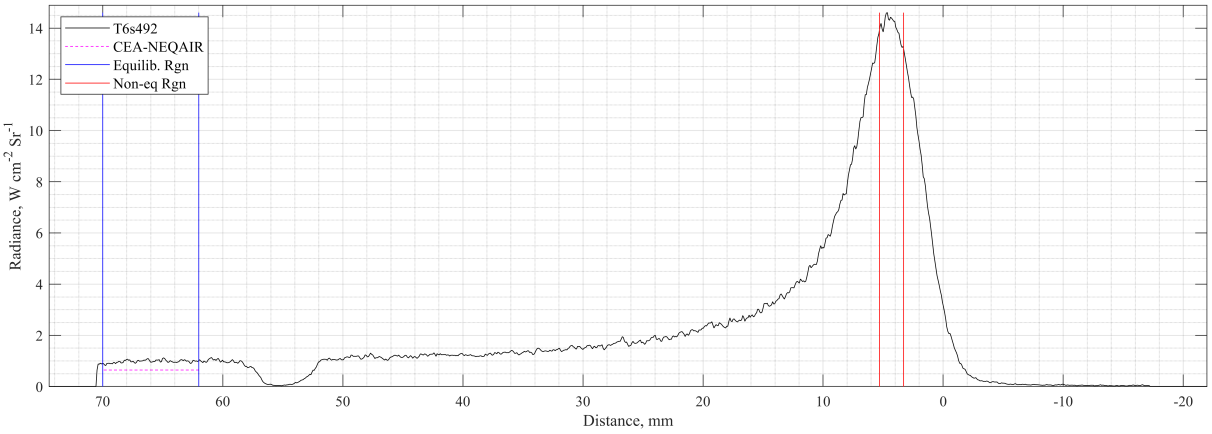

(a) T6s492: Radiance profile integrated over 290 - 520 nm.

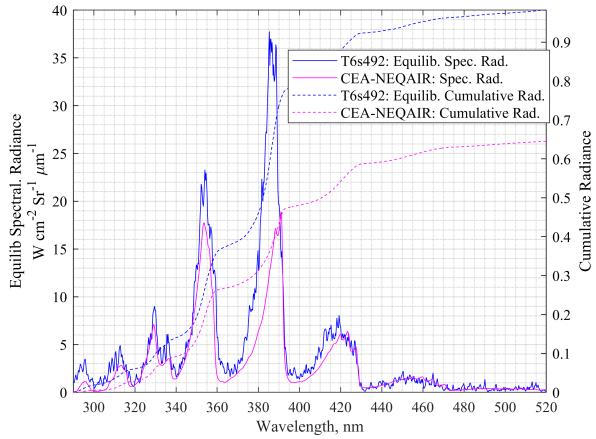

(b) T6s492: Relaxed

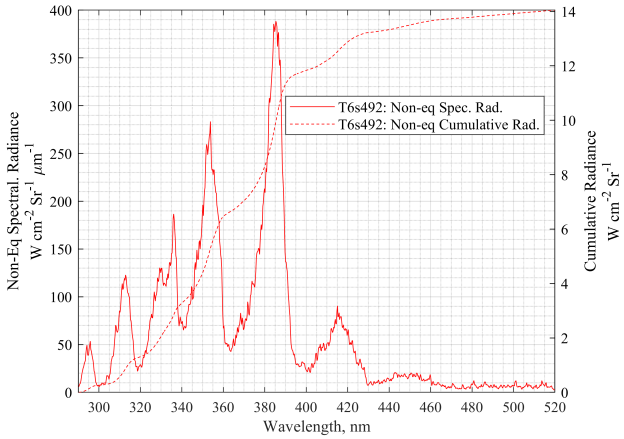

(c) T6s492: Non-equilibrium

Fig. 9 Summary of UV/Vis radiance data from pure nitrogen test case T6s492 (~6.65 km/s at window, 89.95 Pa fill pressure, ~41.5kPa post-shock pressure): (a) Spatial radiance profile integrated over 290 to 520 nm with vertical lines indicating regions chosen to average spectral radiance after relaxation (b) and over non-equilibrium peak (c)

B. Stray Light and Shock Deceleration

The calibration process for absolute radiation measurements has been well document by Cruden [1], and is applied to data acquired from EAST. The same methodology has been applied to the data presented herein, from the T6 Aluminium Shock Tube. As part of the calibration process, stray light must be removed from each calibration and shot image to prevent signal appearing from locations where it did not originate. Traditionally, in shock tube experiments, stray light is taken some distance ahead of the shock front and subtracted everywhere else, as a smooth function dependent on wavelength. Alternatively, plasma torches traditionally look into a wavelength region where there should be no signal, by either looking into VUV wavelengths without a vacuum, or use of a notch filter. The notch filter method has also been trialled in EAST test cases [29]. Comparison of the two methods applied to shock tube data have been made by Glenn et al. [30]. During the recent T6 AST campaign, an alternative stray light removal method where a portion of the signal is blocked both spatially and spectrally was trialled, in the shot images. This provides information of both the spectral and spatial profile of stray light, which is used to generate a "stray light surface" which is subtracted from the raw signal map, before dividing by the calibration surface. Data from the recent campaign has therefore been calibrated using: 1. the traditional method of looking ahead of the shock front (termed the "pre-shock" method here) and 2. the "stray light surface" method, generated from purposely blocking signal within the points of interest. After a few trials,

the stray light surface method only seemed to make a noticeable difference in the UV/Vis data (thought to be owed to higher signal levels for the given test cases) and so was not used on the Vis/NIR channel, to avoid blocking signal.

The UV/Vis radiance profile of high pressure test case T6s496 (~6.85 km/s, 175 Pa fill and ~91.7 kPa post-shock) from 290 to 520 nm is plotted in Figure 10a for both stray light removal methods. It is apparent that the stray light surface method subtracts more signal at all spatial locations by about 5%, and thus has a larger impact in the non-equilibrium region. This result is consistent across all test cases and hypothesised to be due to stronger signal at this location, resulting in more intense stray light surrounding it. This may be an important consideration when studying the relaxation region and extracting rates of the thermochemical reactions. The methodology and results will be described and studied in more detail in future work. In the following sections, data from the traditional "pre-shock" method is used to compare the new T6 AST data to that from the previous campaign and the Electric Arc Shock Tube (EAST) at NASA Ames, so that all have been calibrated using the same methodology.

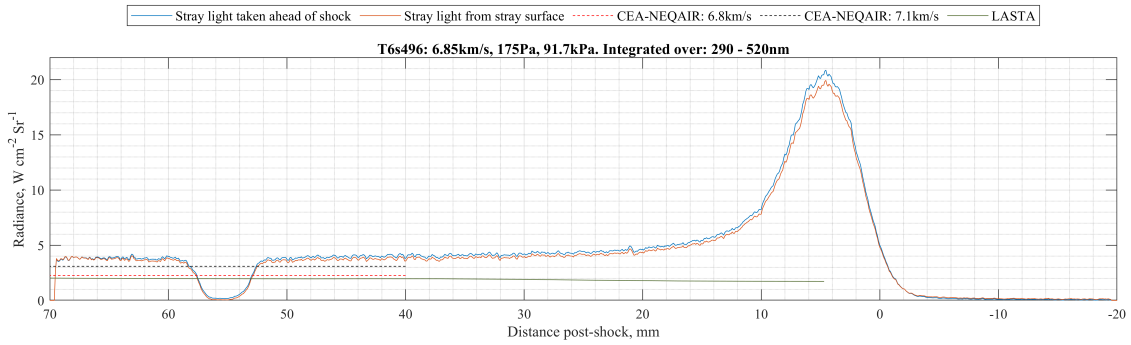

(a) Radiance profiles for T6s496 with alternative stray light removal methods applied. CEA-NEQAIR cumulative radiance results for 6.8km/s and 7.1km/s and LASTA-NEQAIR are also plotted for comparison.

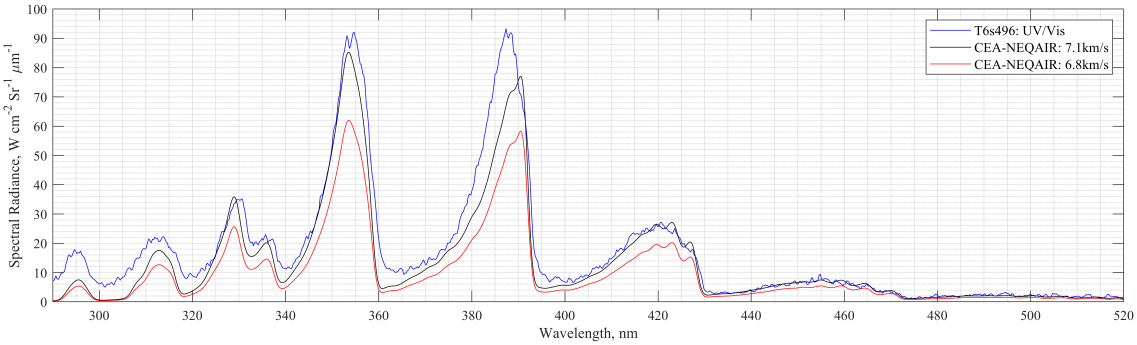

(b) T6s496 UV/Vis spectral radiance from the "pre-shock" method compared against the convolved spectral profiles from CEA-NEQAIR run at 6.8 km/s and 7.1 km/s

Fig. 10 Comparison of T6s496 UV/Vis radiance both spatially (a) and spectrally (b) for different stray light removal techniques, as well as LASTA- and CEA-NEQAIR simulations to assess the effect of varying shock speed.

Finally, a LASTA [20, 21] comparison is also plotted in Figure 10a. This indicates the influence of shock speed variations over the observable test slug. Additionally, CEA-NEQAIR simulations were run at 6.8 and 7.1 km/s - judged to be the minimum and maximum shock speeds just before the window and likely to have processed test gas in the equilibrium region at the time of camera gating. The discrepancy between CEA and LASTA may be due to LASTA using an alternative in-house equilibrium solver: OCEAN. Regardless, both codes result in some variation of the predicted equilibrium radiance when fed into NEQAIR. The spectral profiles are also plotted in Figure 10b. It's evident that the 7.1 km/s simulation is much closer to the measured spectrum, which in part will be due to the higher resulting post-shock pressure (95 kPa vs 87 kPa) and thus higher number densities. Since T6s496 has the strongest amount of shock deceleration of all T6 AST data presented herein, it's concluded that shock speed variation effects will likely warrant consideration for at least some of the test cases in future analysis. However, both simulation results have a strong offset emerging below ~320 nm, which is demonstrated to be typical of high pressure test cases in Section VI.C.

VI. Equilibrium Spectral Comparison

As explained in Section IV, test cases with various post-shock pressures were targeted for this campaign, to enable the study of the thermochemical relaxation at different resolutions. Although the ultimate goal of this work is to provide non-equilibrium data, it must first be demonstrated that experimental and numerical equilibrium data agree. This allows validation of the radiation measurement and calibration process against the radiative numerical modelling, and vice versa. After confirming that these are in close agreement, the additional complication of chemical kinetics can be introduced, knowing that both experiment and numerical results reach the same final equilibrium solution. Chemical rates can then reliably be tuned against the experimental data spatial radiance profiles.

This section performs comparisons of equilibrium spectral radiance from the new T6 AST dataset against that of previous low-speed datasets in both T6 [6] and EAST (Test Release 59) [13], for a number of high and low pressure test cases in synthetic air and pure nitrogen. Simulation results from NASA CEA-NEQAIR (v15.1) codes [26–28] are provided as a common reference based on equilibrium and Boltzmann distribution assumptions. These are convolved with the Instrument Line Shape (ILS) function appropriate to each spectral channel, enabling like-for-like comparison and are used to normalise the experimental spectra to aid comparisons.

A. Comparison to Previous T6 AST Data

Here, data from the new T6 AST dataset is compared against that of the previous dataset [6]. The test cases chosen are: 1. high pressure in pure nitrogen and 2. mid pressure in synthetic air. This is intended to demonstrate the improved agreement between the new experimental data and CEA-NEQAIR simulations across a range of conditions, without having to consider every single test case. Figures 11 and 12 both demonstrate excellent agreement in the Vis/NIR region. This is typical for all test cases in the new T6 AST dataset obtained with a narrow slit width. While an increased offset is still present at higher wavelengths, particularly for the high pressure tests, shown to be very evident in Figure 11c. Additional offsets are present locally due to contaminants such as CN at ~350 and ~390 nm, Aluminium lines just below 400 nm and a sodium line just within view of T6s207 air data at 589 nm.

1. High Pressure Pure Nitrogen

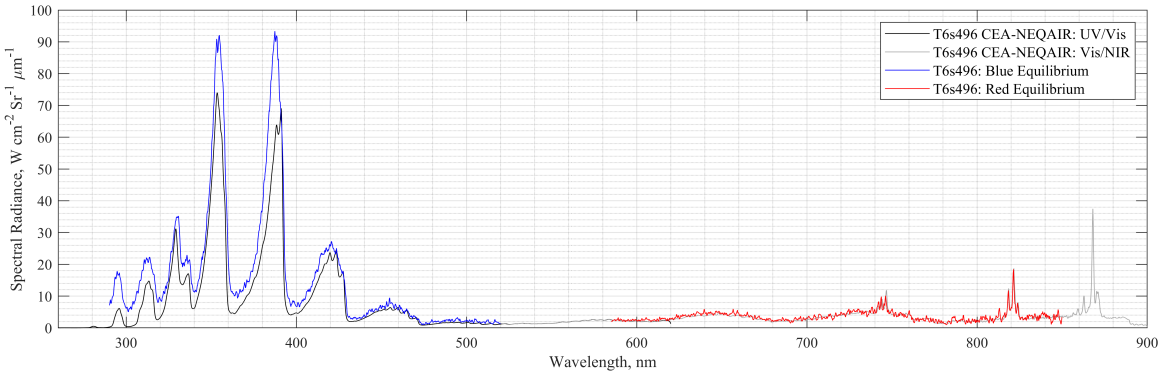

(a) T6s496: Equilibrium spectral radiance plots vs CEA-NEQAIR

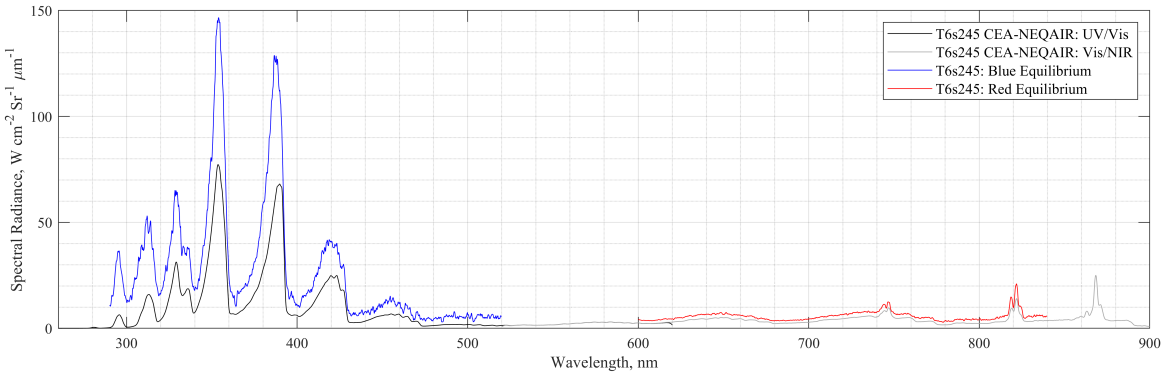

(b) T6s245: Equilibrium spectral radiance plots vs CEA-NEQAIR

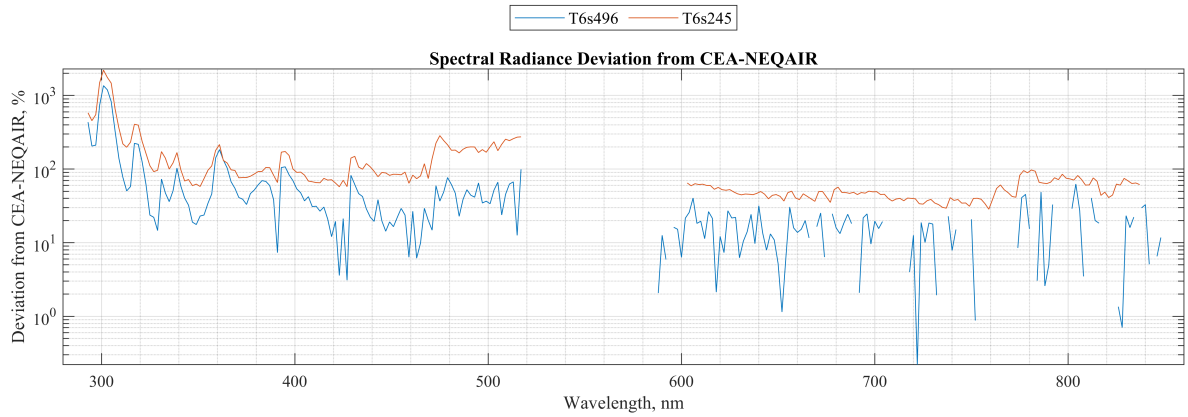

(c) Percentage difference of measured spectral radiance from CEA-NEQAIR prediction for new T6s496 and old T6s245 data. The signal has been binned across 2 mm regions to reduce noise.

Fig. 11 Comparison of UV/Vis and Vis/NIR spectral radiance captured for T6s496 (6.85 km/s at window, 175 Pa fill, ~91.7 kPa post-shock) and T6s245 (6.84 km/s at window, 201 Pa fill, ~105 kPa post-shock). Spectra averaged over the equilibrium region are compared against CEA-NEQAIR results convolved with appropriate instrument line shape for each spectral channel. Gaps in the plots are due to negative numbers on a logarithmic y axis.

2. Mid Pressure Synthetic Air

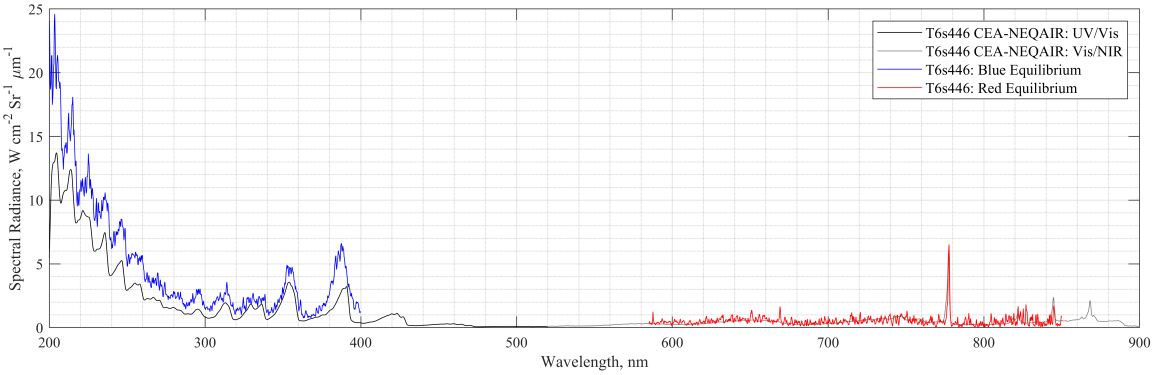

(a) T6s446: Equilibrium spectral radiance plots vs CEA-NEQAIR

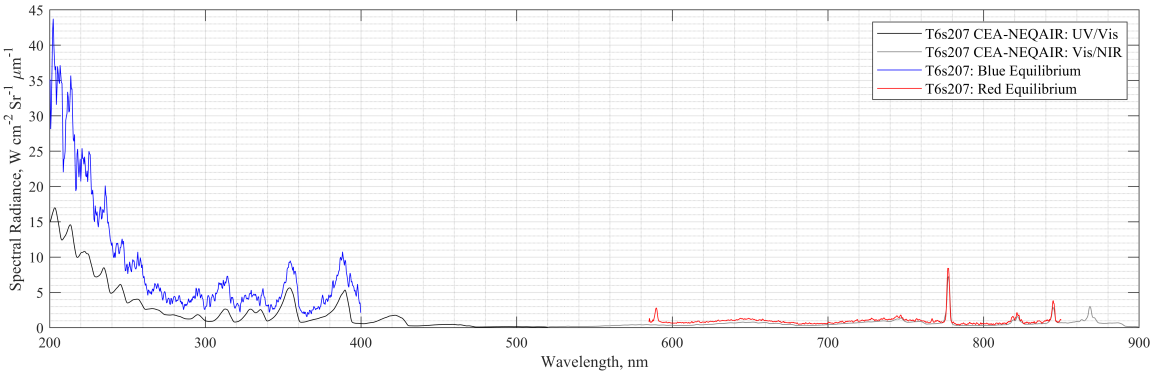

(b) T6s207: Equilibrium spectral radiance plots vs CEA-NEQAIR

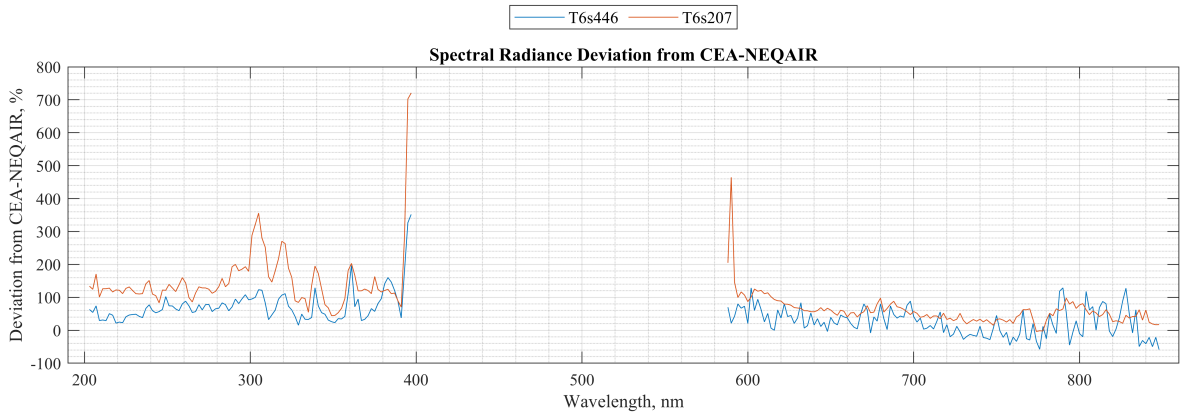

(c) Percentage difference of measured spectral radiance from CEA-NEQAIR prediction for new T6s446 and old T6s207 data. The signal has been binned across 2 mm regions to reduce noise.

Fig. 12 Comparison of UV/Vis and Vis/NIR spectral radiance captured for T6s446 (6.3 km/s at window, 107 Pa fill, ~49.5 kPa post-shock) and T6s207(6.64 km/s at window, 107 Pa fill, ~50 kPa post-shock). Spectra averaged over the equilibrium region are compared against CEA-NEQAIR results convolved with appropriate instrument line shape for each spectral channel.

B. Comparison to EAST Data

As mentioned previously, shock speed variations result in thermochemical gradients in the resulting test slug. It is evident that the EAST test cases in this section have more shock deceleration than their equivalent T6 AST tests (see shock speed profiles in the Appendix). Thus, they have stronger variations through the resulting test slug, as can be seen in the example radiance profile plotted in Figure 13. This may provide an unfair weighting, causing the EAST equilibrium spectra to deviate further from the CEA-NEQAIR simulations, which have been run with shock speeds relevant to near the window. To minimise this effect, spectra were averaged in the lowest regions of the resulting radiance profiles in all channels, as indicated in Figure 13. Comparisons of equilibrium spectra from EAST shots 59-47 and 59-42 are made to equivalent conditions from the new T6 AST dataset at mid pressure and low pressure in synthetic air.

The new T6 AST equilibrium spectra compare against CEA-NEQAIR predictions better than both EAST tests in the Vis/NIR (or "Red channel"). At both conditions, the EAST Vis/NIR spectra show a strong deviation from CEA-NEQAIR below 600 nm and do not agree with the calibrated UV/Vis data (or "Blue channel"). Spectral channels not agreeing is an indication the calibrated data is wrong at for at least one of them. It's evident from the width of the atomic lines in the EAST Vis/NIR data that wide spectrometer slit widths have been used. This supports the argument given in Section III.B, that wide slit widths result in calibrated spectra vertically offset from CEA-NEQAIR predictions.

The mid pressure test cases, T6s446 and EAST-59-47, compare similarly against CEA-NEQAIR in the UV/Vis region. The Instrument Line Shape (ILS) of the EAST Blue spectral channel is approximately one quarter of that for the Red channel. This suggests a narrower slit width, which again coincides with better agreement to CEA-NEQAIR prediction. An increased offset just below 400 nm is evident in the T6 AST data due to Aluminium contamination. Otherwise, the close agreement of the test cases against CEA-NEQAIR predictions is very good. For the low pressure EAST test case, EAST-59-42, the UV/Vis baseline offset from CEA-NEQAIR is approximately the same as mid pressure case EAST-59-47. Though for T6s483 low pressure case this baseline is reduced, with the main offsets located at ~280 to ~320 nm and ~390 nm. These elevated offsets also appear in the EAST-59-42 data, in addition to a carbon line emerging at ~247 nm. The 390 nm offset is due to CN, resulting from carbon contamination. The source of the offset from ~280 to ~320 nm is currently unknown, though is common in both T6 and EAST data for both synthetic air and pure nitrogen test cases. Given the better agreement either side of this offset, it is believed to be a physical result, rather than a calibration artefact.

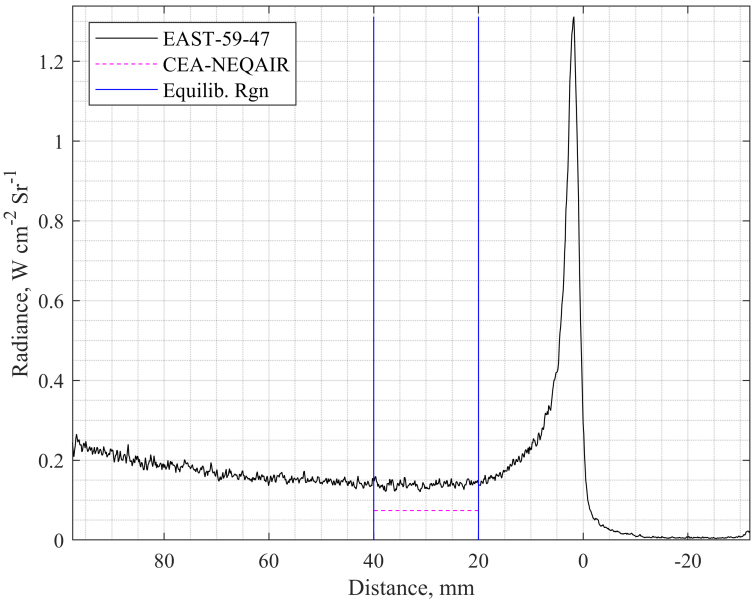

Fig. 13 Radiance profile for EAST-59-47 Blue channel. The plateau averaged over to generate equilibrium spectral radiance is indicated. Location is chosen to minimise shock deceleration effects.

1. Mid Pressure Synthetic Air

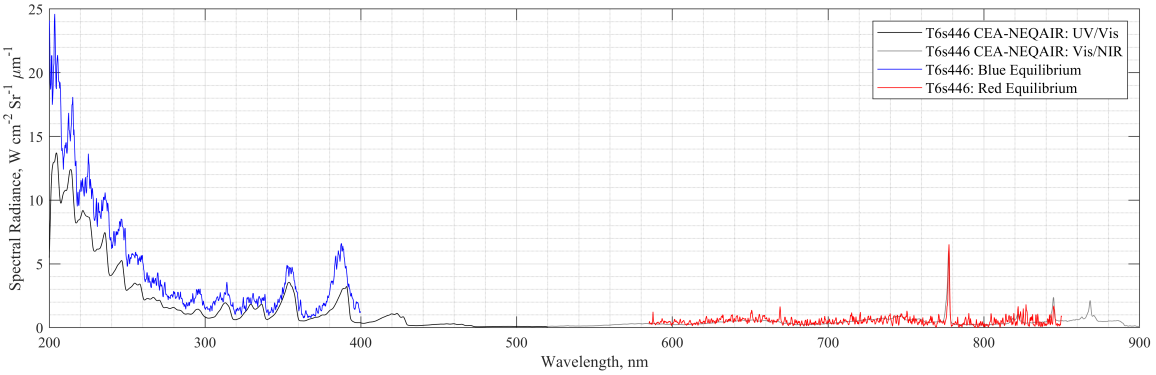

(a) T6s446: Equilibrium spectral radiance plots vs CEA-NEQAIR

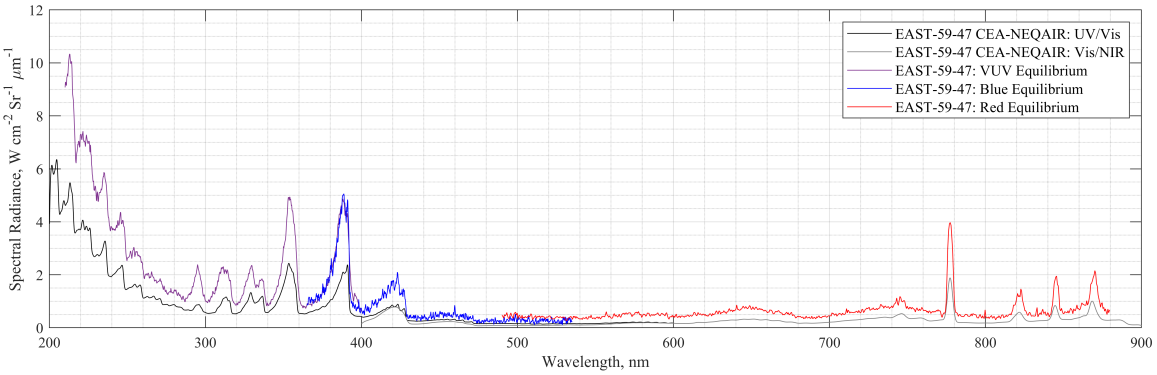

(b) EAST-59-47: Equilibrium spectral radiance plots vs CEA-NEQAIR

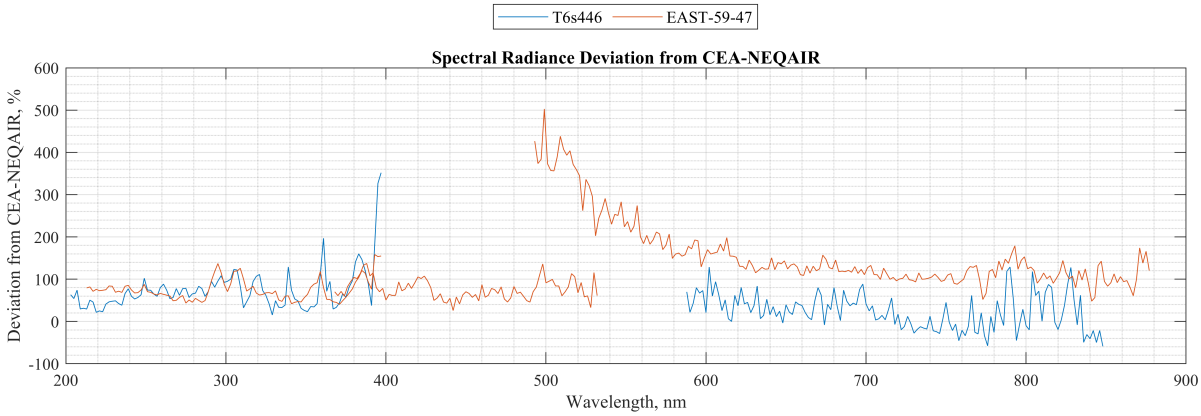

(c) Percentage difference of measured spectral radiance from CEA-NEQAIR prediction for new T6s446 and EAST-59-47 data. The signal has been binned across 2 mm regions to reduce noise.

Fig. 14 Comparison of UV/Vis and Vis/NIR spectral radiance captured for T6s446 (6.3 km/s at window, 107 Pa fill, ~49.5 kPa post-shock) and EAST-59-47 (6.81 km/s at window, 94.7 Pa fill, ~48.6 kPa post-shock). Spectra averaged over the equilibrium region are compared against CEA-NEQAIR results convolved with appropriate instrument line shape for each spectral channel.

2. Low Pressure Synthetic Air

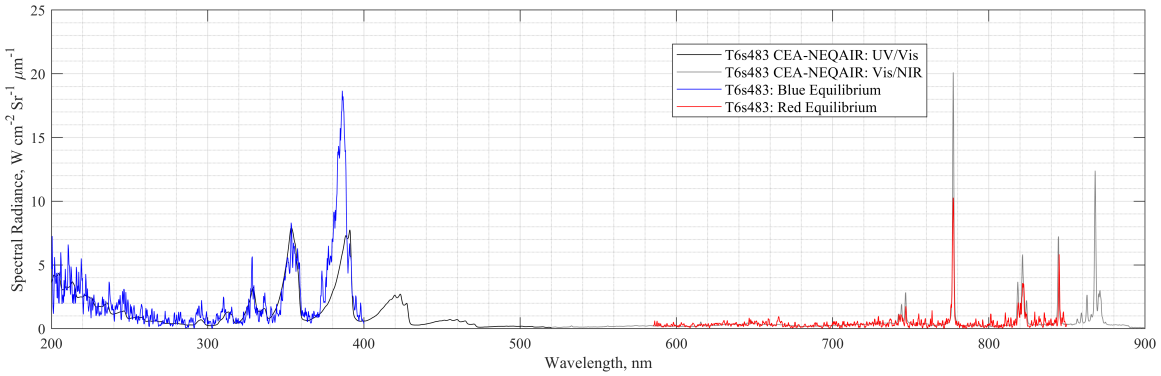

(a) T6s483: Equilibrium spectral radiance plots vs CEA-NEQAIR

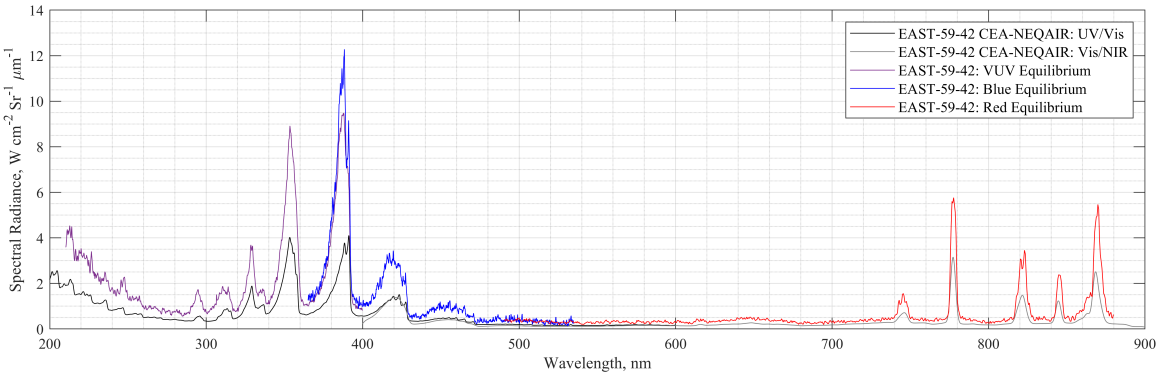

(b) EAST-59-42: Equilibrium spectral radiance plots vs CEA-NEQAIR

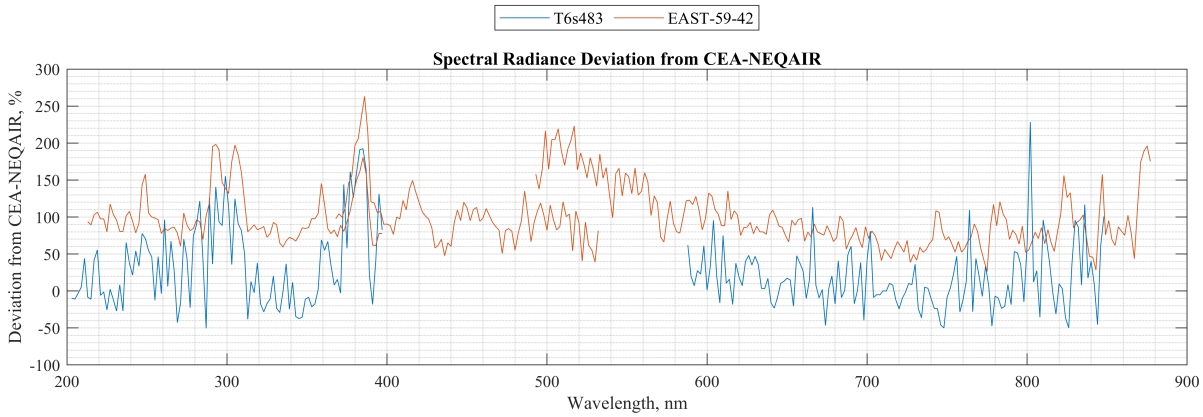

(c) Percentage difference of measured spectral radiance from CEA-NEQAIR prediction for new T6s483 and EAST-59-42 data. The signal has been binned across 2 mm regions to reduce noise.

Fig. 15 Comparison of UV/Vis and Vis/NIR spectral radiance captured for T6s483 (8.0 km/s at window, 33 Pa fill, ~23.4 kPa post-shock) and EAST-59-42 (8.09 km/s at window, 40 Pa fill, ~29.2 kPa post-shock). Spectra averaged over the equilibrium region are compared against CEA-NEQAIR results convolved with appropriate instrument line shape for each spectral channel.

C. Comparison of New T6 AST: High Pressure vs Low Pressure

This section compares synthetic air and pure nitrogen spectra generated in high pressure and low pressure test cases, processed by shockwaves with a similar speed at the windows. It is noted that the radiance profiles of the low pressure cases T6s494 and T6s484, in pure nitrogen and synthetic air respectively, don't quite fully relax in the optics FOV. UV/Vis and Vis/NIR spatial radiance profiles for the low pressure pure nitrogen data are plotted in Figure 16 to illustrate this. Spectra for the low pressure cases are thus averaged over regions still relaxing. Additionally, the signal level in the Vis/NIR data relaxes to not much above the noise, thus averaging into the relaxation region is necessary to attain a discernible signal above that of the remaining noise level. Since the low pressure test cases have not fully equilibrated, the spectra generated would not be expected to agree with CEA-NEQAIR predictions.

In both pure nitrogen and synthetic air comparisons, specific deviations from CEA-NEQAIR predictions are revealed at high pressure and low pressure extremes. At higher pressures, there is an exaggerated offset from CEA-NEQAIR predictions in the lower wavelengths, typically starting around ~320 nm for both gas mixtures. This is believed to be physical, and potentially the result of a background radiation source such as Bremsstrahlung radiation [25], rather than an excess of NO species (since it is present in the pure nitrogen test cases). Conversely, at lower pressures the contaminants make up a larger mole fraction of the test gas and thus the CN radiation increases in dominance in the UV/Vis spectra. Hence, increased offsets at~350 and ~390 nm are evident in both gas mixtures at lower pressure conditions.

Interestingly, for both high and low pressure synthetic air cases, Figure 18c shows the deviation from CEA-NEQAIR peaks at ~300 nm, as is the case for the pure nitrogen data in Figure 17c, but then decreases gradually at lower wavelengths. Additionally, the magnitude of deviations from the CEA-NEQAIR simulation in the synthetic air is an order of magnitude less than that in the pure nitrogen cases. This is likely due to the pure nitrogen CEA-NEQAIR simulations predicting essentially zero radiance at ~285 and ~300 nm, where it appears as if a background radiation source (e.g. Bremsstrahlung [25]) has not been included.

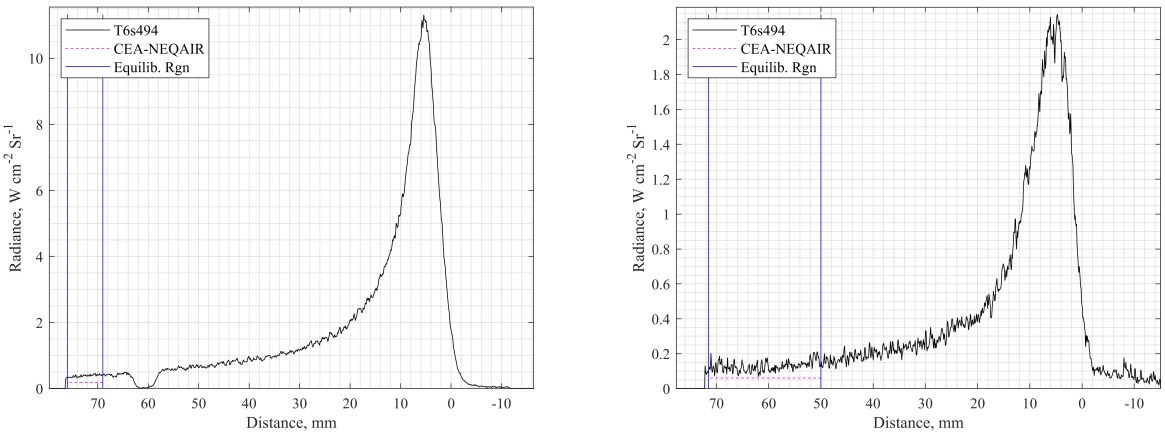

(a) UV/Vis: 290-520 nm **(b) Vis/NIR: 585 - 850 nm**

Fig. 16 Radiance profiles of T6s494 in the (a) UV/Vis and (b) Vis/NIR. The test slug didn't reach full relaxation in either channel

1. Pure Nitrogen

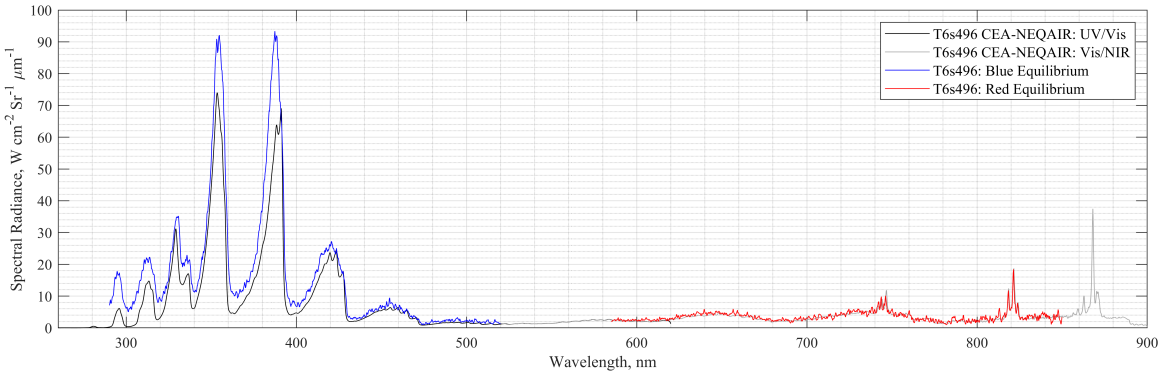

(a) T6s496: Equilibrium spectral radiance plots vs CEA-NEQAIR

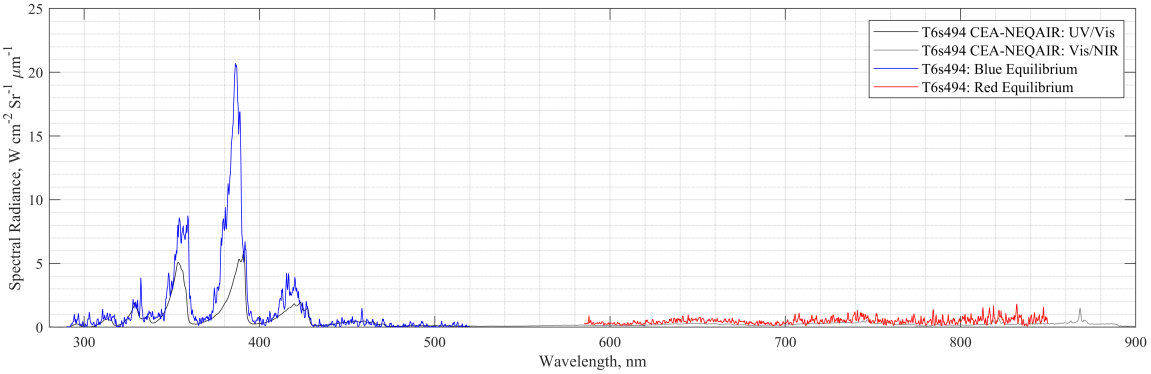

(b) T6s494: Equilibrium spectral radiance plots vs CEA-NEQAIR

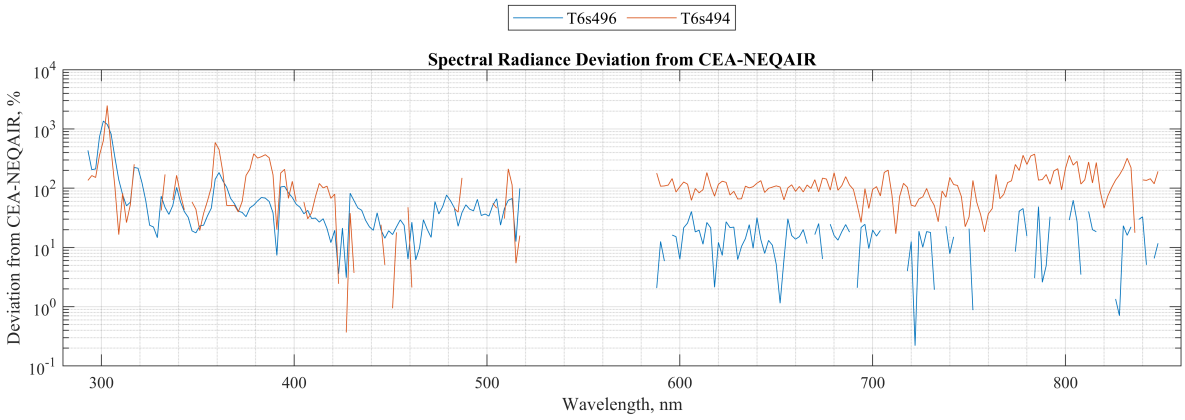

(c) Percentage difference of measured spectral radiance from CEA-NEQAIR prediction for new T6s496 and T6s494 data. The signal has been binned across 2 mm regions to reduce noise.

Fig. 17 Comparison of UV/Vis and Vis/NIR spectral radiance captured for T6s496 (6.85 km/s at window, 175 Pa fill, ~91.7 kPa post-shock) and T6s494 (6.6 km/s at window, 40.5 Pa fill, ~19.5 kPa post-shock). Spectra averaged over the equilibrium region are compared against CEA-NEQAIR results convolved with appropriate instrument line shape for each spectral channel. Gaps in the plots are due to negative numbers on a logarithmic y axis.

2. Synthetic Air

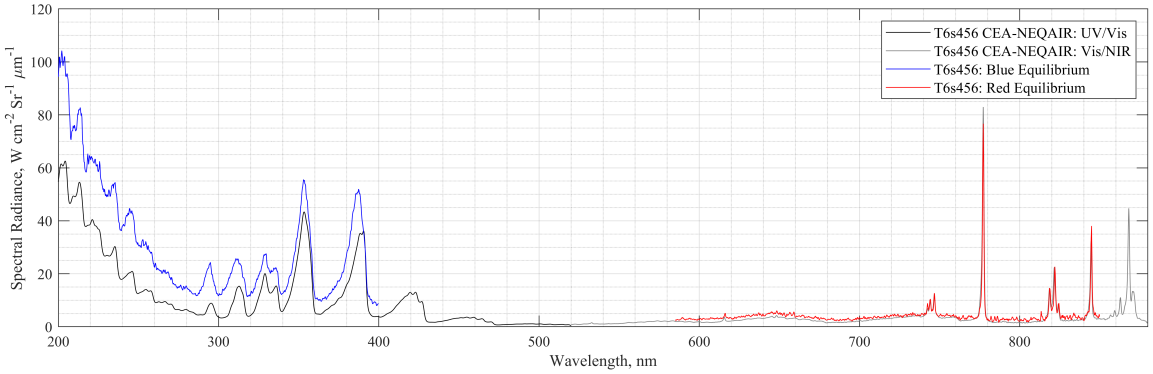

(a) T6s456: Equilibrium spectral radiance plots vs CEA-NEQAIR

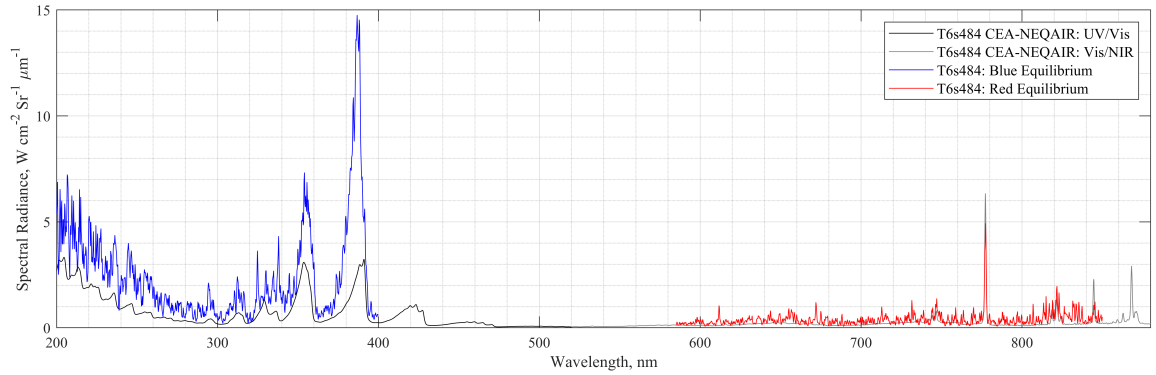

(b) T6s484: Equilibrium spectral radiance plots vs CEA-NEQAIR

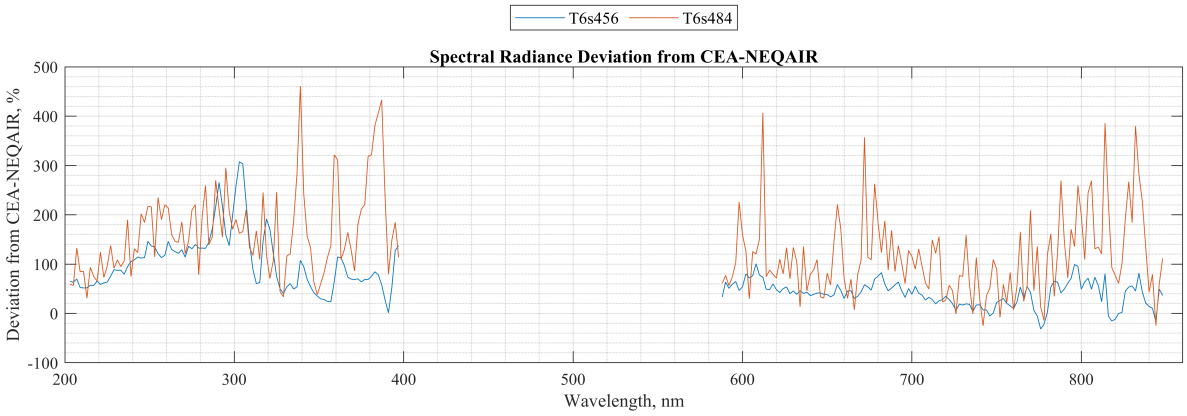

(c) Percentage difference of measured spectral radiance from CEA-NEQAIR prediction for new T6s456 and T6s484 data. The signal has been binned across 2 mm regions to reduce noise.

Fig. 18 Comparison of UV/Vis and Vis/NIR spectral radiance captured for T6s456 (7.26 km/s at window, 175 Pa fill, ~105.1 kPa post-shock) and T6s484 (7.3 km/s at window, 33.3 Pa fill, ~20.6 kPa post-shock). Spectra averaged over the equilibrium region are compared against CEA-NEQAIR results convolved with appropriate instrument line shape for each spectral channel.

VII. Non-Equilibrium Radiation

In this section, first, pure nitrogen radiance profiles are plotted to compare non-equilibrium relaxation as a function of: 1. shock speed (for cases with a similar post-shock pressure) and 2. post-shock pressure (for cases with a similar shock speed at the window). Plots for all cases are integrated from 290 to 520 nm in the UV/Vis and 585 to 850 nm in the Vis/NIR region, thus encapsulating a variety of molecular and atomic species. The second part of this section looks at the spectral evolution at varying points through the test slug of a low pressure synthetic air test case.

A. Pure Nitrogen Radiance Profiles

1. ~44 kPa Post-Shock Test Cases

Figure 19 compares test cases at similar post-shock pressures (~41.5 to ~47 kPa) with shock speeds varying from 6.2 to 7.4 km/s at the window. In both spectral regions, as shock speed increases, so do both the equilibrium and non-equilibrium radiance. All appear to just about fully relax by the end of the visible test slug. Additionally, when normalised by the peak non-equilibrium radiance, the radiance profiles align quite well, with the relative heights of the non-equilibrium and equilibrium region being common to all cases, for both spectral channels. This also indicates the relaxation rates vary little with shock speed (and therefore post-shock temperature) over this relatively narrow shock speed range.

As mentioned previously, the non-equilibrium peak was chosen to normalise the radiance profiles (over the equilibrium region) since for many lower pressure cases, the end of relaxation was not visible in the telecentric optics FOV. Additionally, the spatial smear convolution functions should be very similar across all test cases, which supports the non-equilibrium peak to be a viable point to normalise all test cases against.

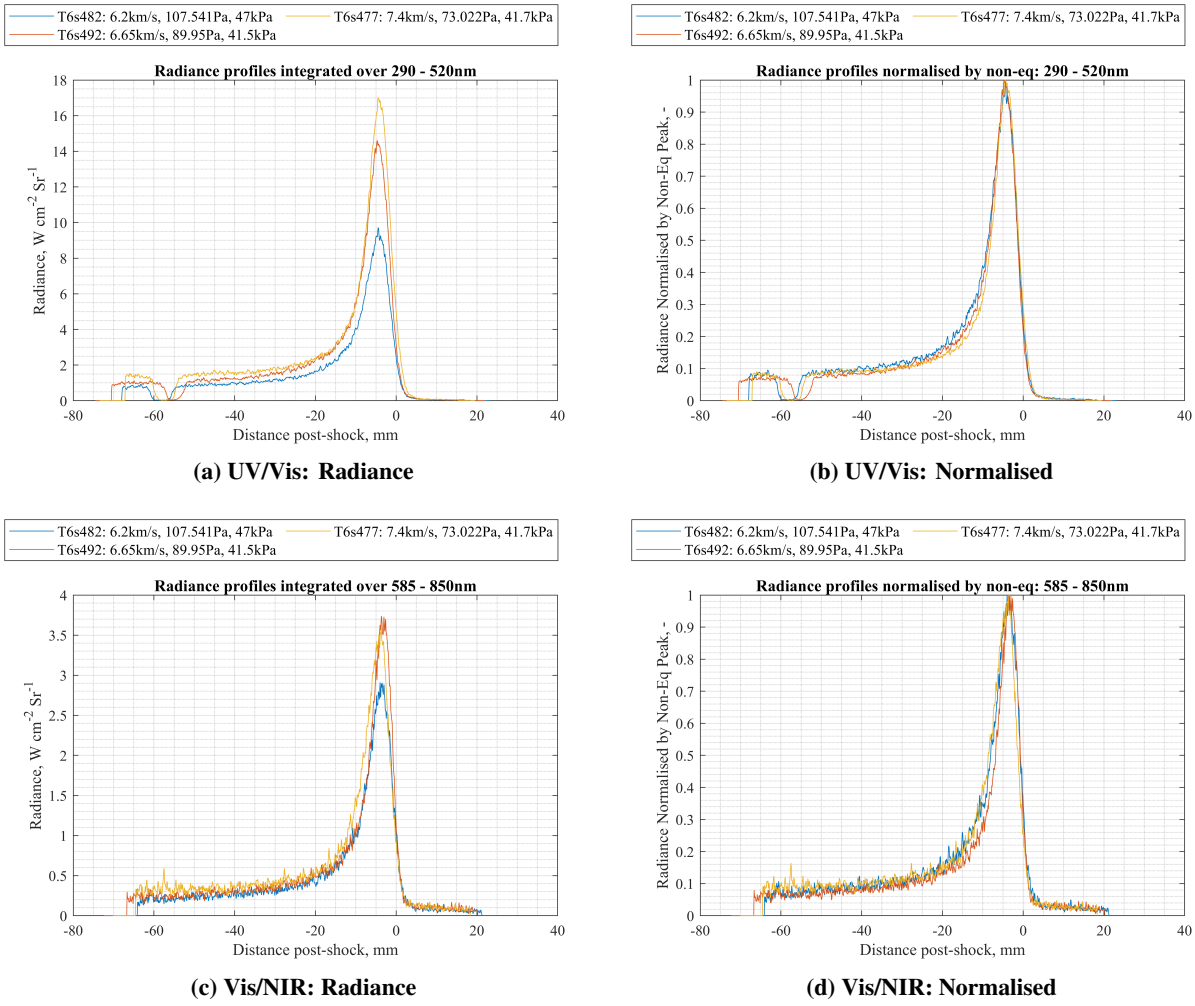

(a) UV/Vis: Radiance **(b) UV/Vis: Normalised**

(c) Vis/NIR: Radiance **(d) Vis/NIR: Normalised**

Fig. 19 Calibrated radiance profiles (left) and radiance profiles normalised by non-equilibrium peak (right), for test cases all with post-shock pressure near ~44 kPa but different shock speeds, integrated across 290-520nm (top) and 585-850 nm (bottom).

2. ~6.7 km/s Test Cases

Decreasing post-shock pressure results in a much more elongated non-equilibrium region, than decreasing shock speed, in both wavelength regions. This is shown in Figure 20. Furthermore, the ratio of the non-equilibrium region height to the steady equilibrium plateau height increases at lower pressures. Again, the same gating times were used for all test cases in this paper and so the spatial smearing function will be very similar for all - thus the differences in non-equilibrium region length should be due to differences in reaction rates, not smear functions. The lower pressure test case, T6s494, doesn't fully relax to equilibrium within the FOV of the OES setups.

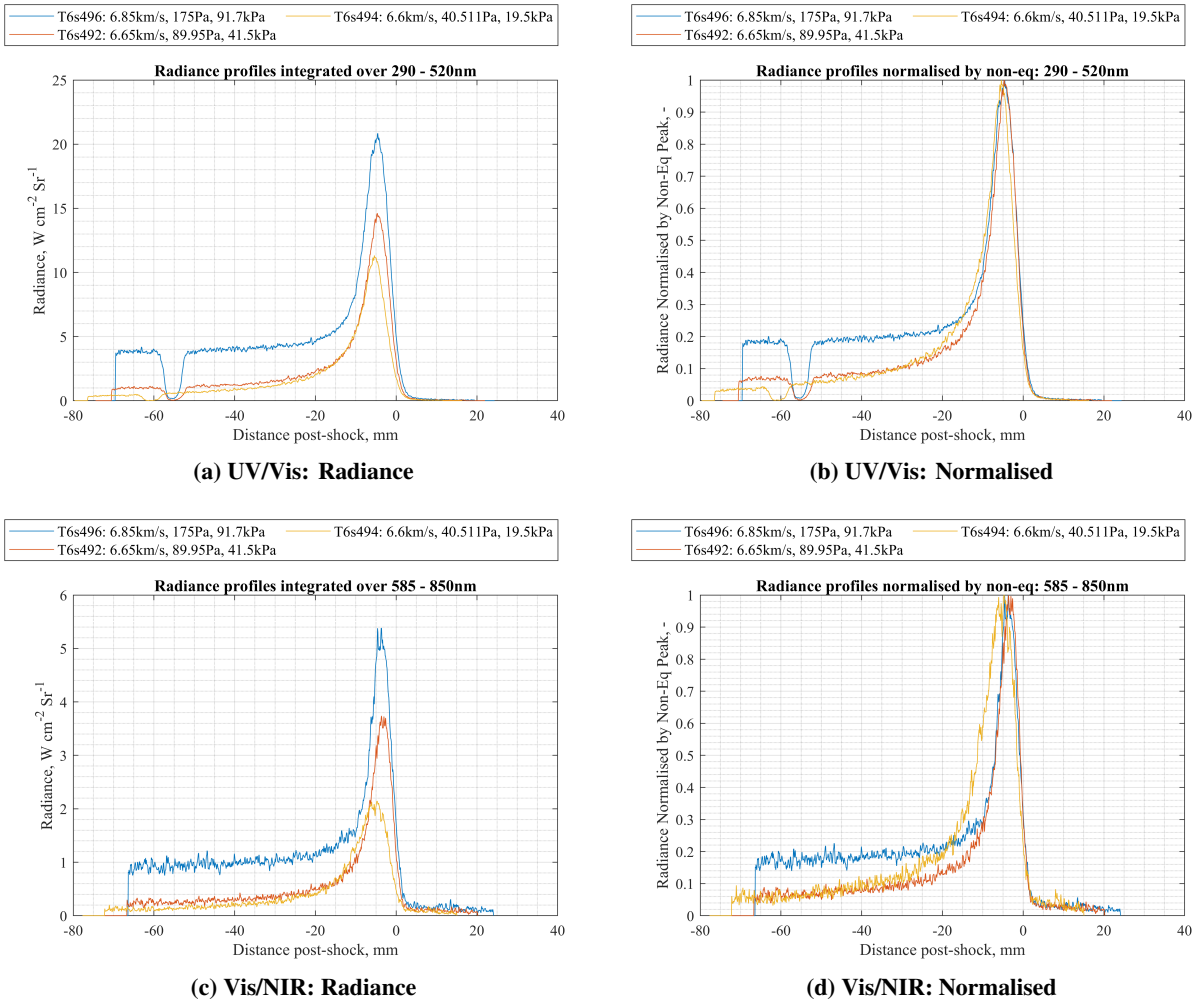

(a) UV/Vis: Radiance **(b) UV/Vis: Normalised**

(c) Vis/NIR: Radiance **(d) Vis/NIR: Normalised**

Fig. 20 Calibrated radiance profiles (left) and radiance profiles normalised by non-equilibrium peak (right), for test cases all with shock speed near 6.7 km/s at window but different pressures, integrated across 290-520nm (top) and 585-850 nm (bottom).

B. Spectral Evolution Through Relaxation Region

Figure 21 plots the spectral radiance evolution through the test slug of low pressure synthetic air test case T6s484 in the UV/Vis region, from 200 to 400 nm. These spectra were averaged over 2 mm regions, centred on the locations indicated in the radiance profile, thus signal-to-noise ratio decreases along the relaxation region. It provides a first look at the rates of how the different species relax progressively from the non-equilibrium peak - seemingly at a quicker rate at the lower wavelengths, perhaps due to rapid NO dissociation. Additionally, the N_2 and N_2^+ band relative heights change rapidly in the first 10 mm behind the shock front. The overall intensity of radiation originating from the non-equilibrium region is nearly two orders of magnitude higher than that near the end of full relaxation. In future work spectral profiles slices, like this example, will be used to perform spectral fitting through the test slug in an attempt to attain temporal variations in number densities and temperatures through the test slug. This will include the assumption of a homogeneous test gas across the diameter of the tube, and thus ignore boundary layer effects.

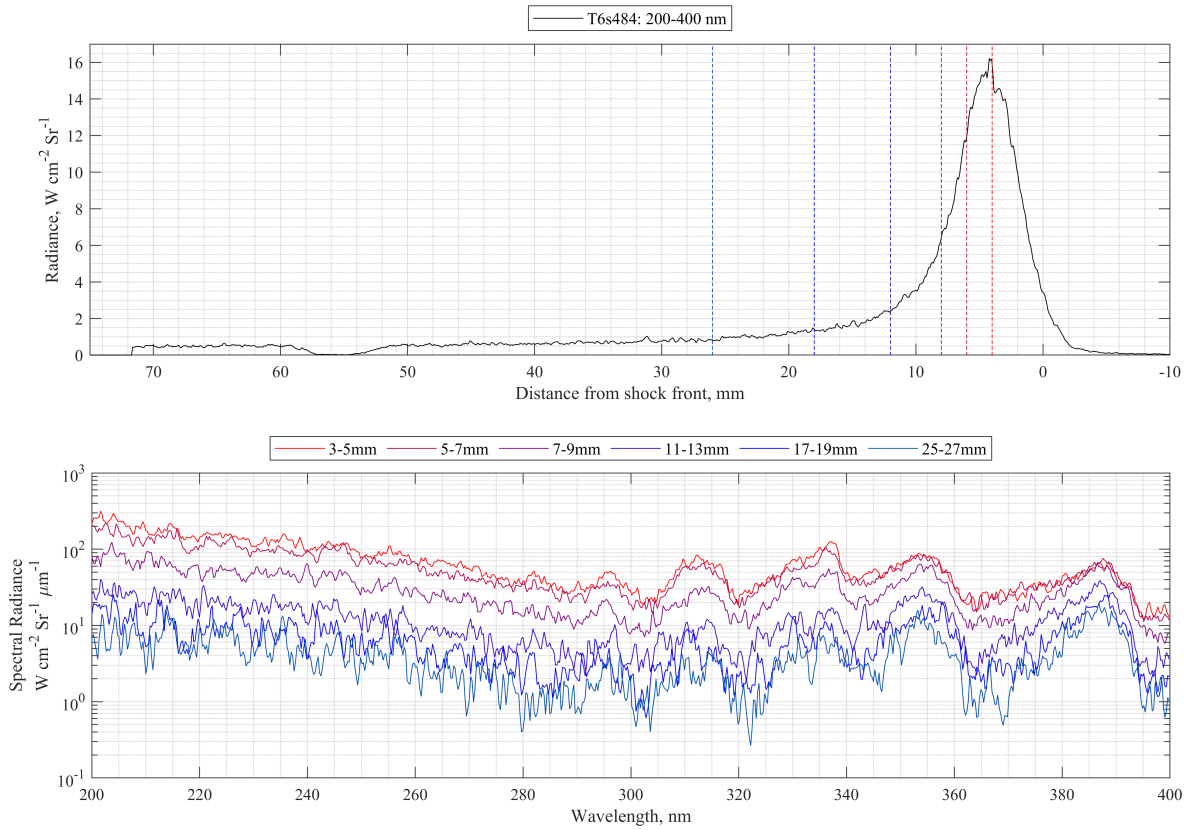

Fig. 21 Summary of UV/Vis spectral radiance plots averaged over 2mm regions at multiple points through the test gas, through the relaxation region, for T6s484 (~7.3 km/s, 33.3 Pa fill, ~20.6 kPa in synthetic air).

VIII. Carbon Contamination

As referred to in Section III.C, cleaning the tube walls to reduce contaminants is an important step performed before each test. The N_2^+ first negative band contains two strong peaks at ~350 and ~390 nm, as seen in many of the previous spectra, including test case T6s484 shown in Figure 21 in the previous section. Radiation for the CN violet can superimpose on these bands in low resolution spectra to make the N_2^+ radiation appear stronger than it is. Large amounts of radiation were measured at these wavelengths, in the non-equilibrium relaxation region of the low pressure shots as previously shown. To distinguish the origin of this radiation (i.e. CN or N_2^+) a 600 groove/mm diffraction grating was installed for T6s501 - intended to be the same test case as T6s484 but with high resolution UV/Vis spectra.

Figure 22 summarises the UV/Vis data from T6s501. It can be seen that spectral resolution is improved at the expense of spectral range. Spectra are averaged at both the far downstream end (which isn't yet fully relaxed) and the non-equilibrium peak. The former is compared to a CEA-NEQAIR simulation, predicting the equilibrium spectral radiance profile for a N_2/O_2 mixture, for the given test case and convolved with the measured ILS. Two large discrepancies are evident - these are a measure of the CN violet superimposing with the rest of the spectrum. It's evident that they make up the majority of the cumulative radiance in this region. Relaxation not yet running to completion can also be contributing to the offset, and maybe promoting the CN radiation further, due to temperatures above that of equilibrium. In any case, it is evident that the presence of even very small amounts of CN can result in large discrepancies in the UV/Vis for low pressures conditions, particularly in the non-equilibrium region. A more detailed study to evaluate the mole fractions of contaminants present in these test cases and their impact on the resulting thermochemistry is made by Clarke et al. [31].

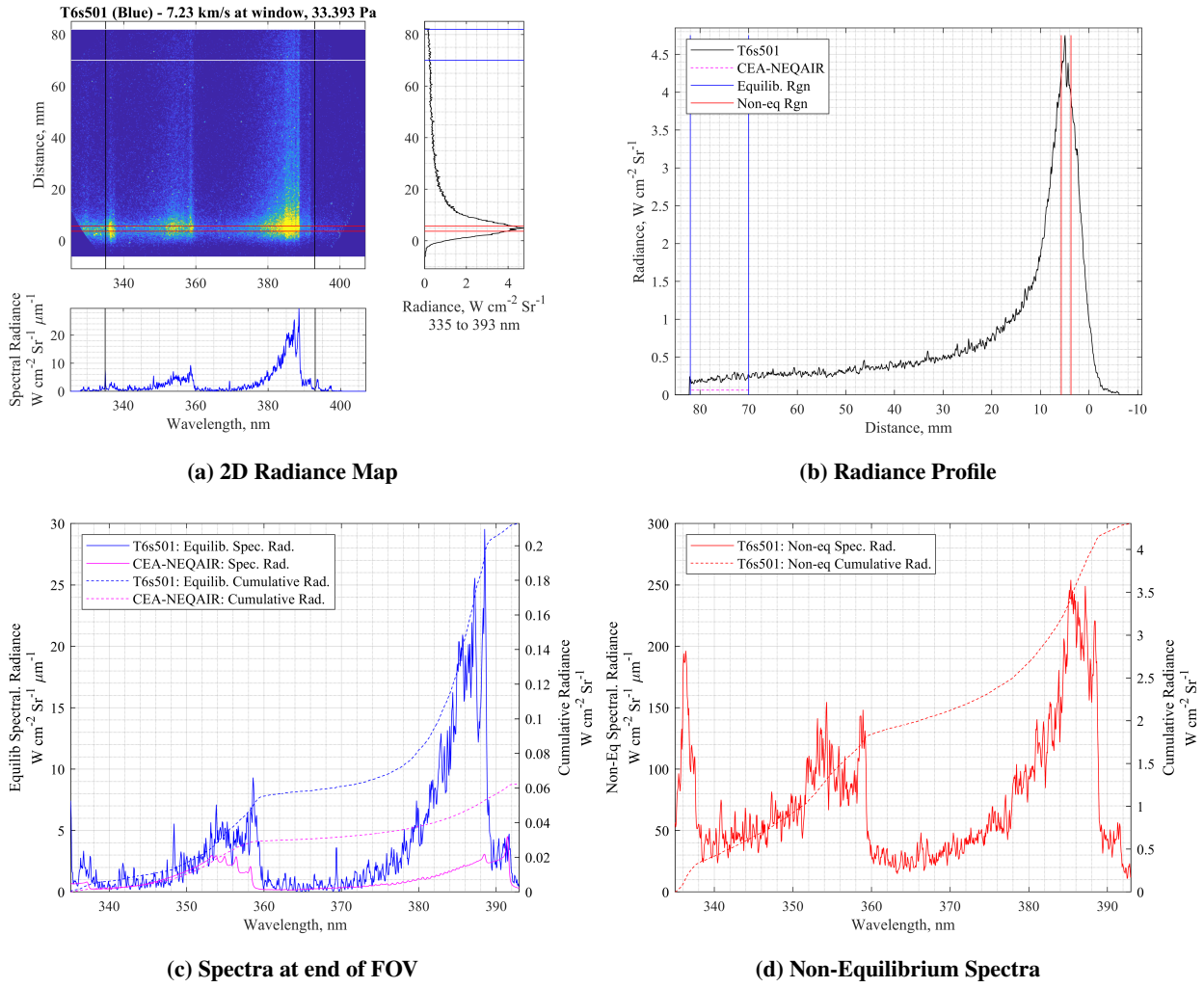

(a) 2D Radiance Map

(b) Radiance Profile

(c) Spectra at end of FOV

(d) Non-Equilibrium Spectra

Fig. 22 Summary of T6s501 (7.23 km/s at window, 33.4 Pa fill, ~20.0 kPa post-shock) high resolution UV/Vis data. The CEA-NEQAIR equilibrium simulation in (c) is run with only N_2 and O_2. The large discrepancies at ~358 and ~378 to ~390 nm are due to CN contaminants in the experimental data.

IX. Conclusion

Absolute radiance of synthetic air and pure nitrogen test cases have been measured in the UV/Vis and Vis/NIR for shock speeds from 5.7 to 8.0 km/s and a range of post-shock pressures in the Oxford T6 Stalker Tunnel while operating in Aluminium Shock Tube mode. Improved agreement of measured equilibrium spectral radiance against CEA-NEQAIR simulation results, compared to previous campaigns in both the T6 and Electric Arc Shock Tube at NASA Ames, has been demonstrated. Narrower spectrometer slit widths is believed to contribute towards these improved agreements, by reducing stray light in the spectrometers. Shock deceleration effects should be accounted for in future analysis for at least some of the test cases. Spatial radiance profiles are plotted and compared as a function of shock speed and post-shock pressure. It is shown that resolution of the non-equilibrium relaxation region can be improved by considering lower pressure test cases. This will be useful in the study of chemical kinetics, to tune reaction rates such that radiance profiles can be replicated by numerical simulations convolved with the correct spatial smear function. Additionally, example spectral slices through a low pressure non-equilibrium region demonstrates the data is viable to attempt spectral fitting in future works to deduce number densities and temperatures throughout the relaxation process. Contamination in the form of cyanogen, CN, is identified across all test cases and may become a limitation when studying the N_2^+ first negative band in the UV/Vis region. Attempts to remove such contaminants will be detailed in future papers. Despite this, the dataset is recommended as a reliable resource which numerical and facility results can be benchmarked against. Future work will involve a more detailed analysis of the experimental data, characterisation of the optical set up (including spectral and spatial smear functions) and application of state of the art codes to see how they fare against this new dataset and test conditions.

Appendix

This section provides the paired shock speed profiles for the equilibrium spectral comparisons in Section VI. Refer to Table 1 in Section IV for additional shot information.

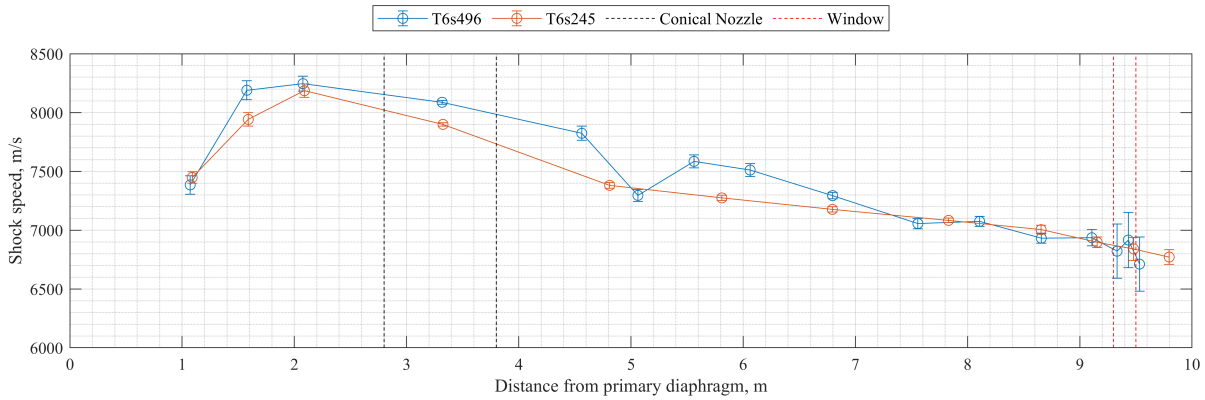

Fig. 23 Shock profiles for high pressure pure nitrogen test cases: T6s496 and T6s245.

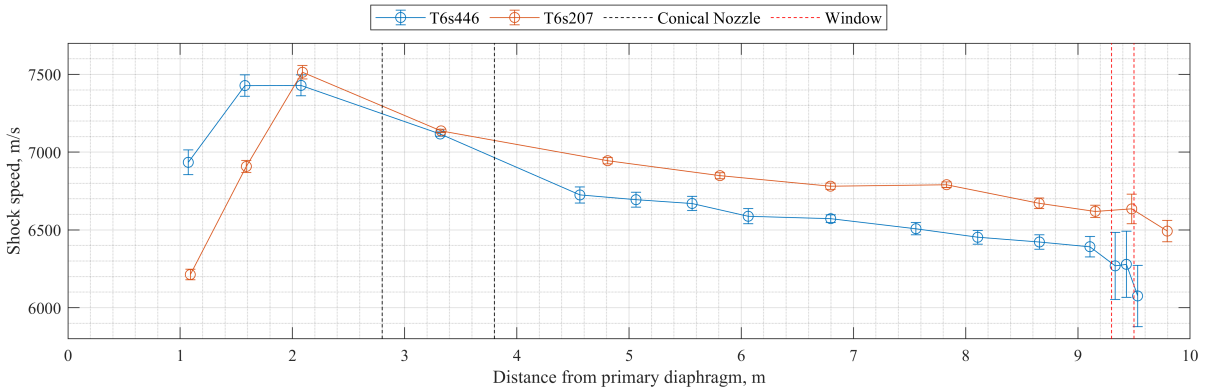

Fig. 24 Shock profiles for mid pressure synthetic air test cases: T6s446 and T6s207.

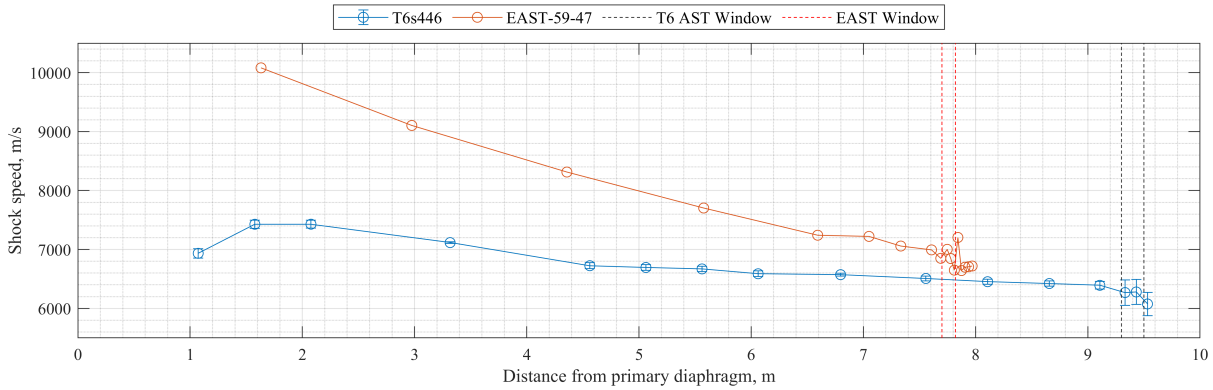

Fig. 25 Shock profiles for mid pressure synthetic air test cases: T6s446 and EAST-59-47.

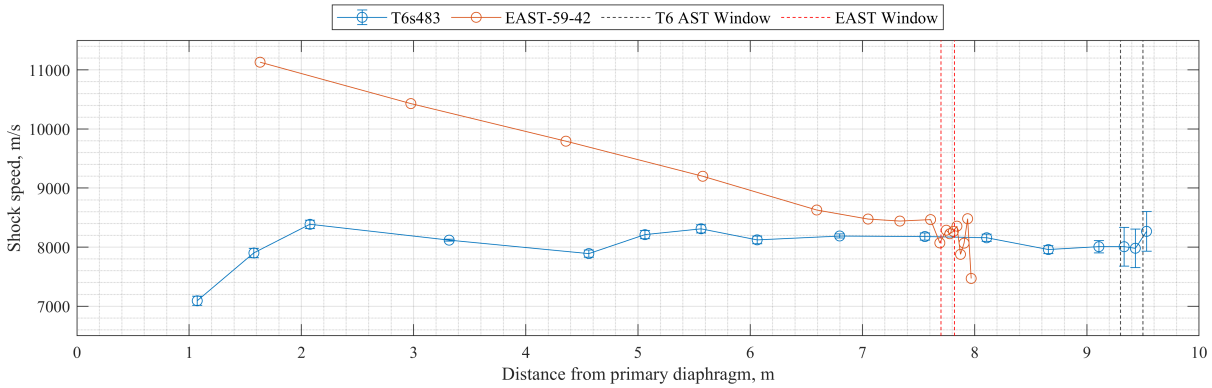

Fig. 26 Shock profiles for low pressure synthetic air test cases: T6s483 and EAST-59-42.

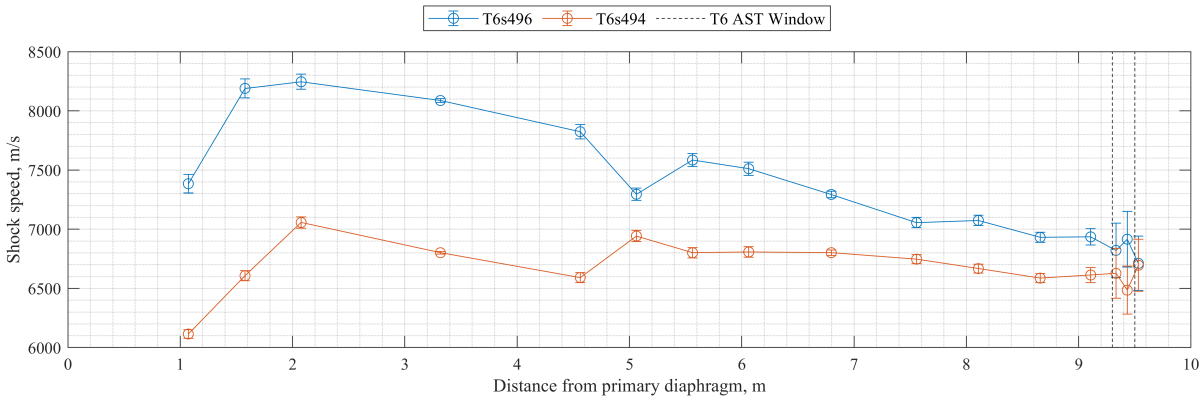

Fig. 27 Shock profiles for high and low pressure pure nitrogen test cases: T6s496 and T6s494.

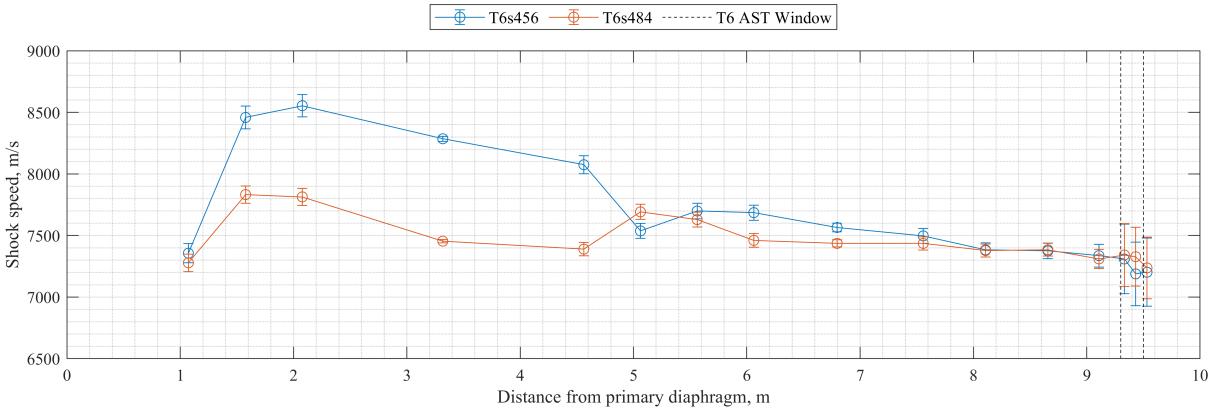

Fig. 28 Shock profiles for high and low pressure synthetic air test cases: T6s456 and T6s484.

Acknowledgments

Data presented from the previous T6 AST campaign was funded by US Air Force grant FA9550-19-1-7020. Additionally, the authors thank Dr Tobias Hermann for the generous loan of the Deuterium calibration lamp.

References

[1] Cruden, B. A., "Absolute radiation measurements in earth and mars entry conditions," 2014.

[2] Laux, C. O., Spence, T., Kruger, C., and Zare, R., "Optical diagnostics of atmospheric pressure air plasmas," *Plasma Sources Science and Technology*, Vol. 12, No. 2, 2003, p. 125.

[3] Collen, P., "Development of a High-Enthalpy Ground Test Facility for Shock-Layer Radiation," Ph.D. thesis, Univ. of Oxford, Oxford, UK, 2021.

[4] Collen, P., Doherty, L. J., Subiah, S. D., Sopek, T., Jahn, I., Gildfind, D., Penty Geraets, R., Gollan, R., Hambidge, C., Morgan, R., et al., "Development and commissioning of the T6 Stalker Tunnel," *Experiments in Fluids*, Vol. 62, No. 11, 2021, pp. 1–24.

[5] McGilvray, M., Collen, P., Doherty, L., Steer, J., Leader, J., Glenn, A., and Hambidge, C., "The Oxford T6 Stalker tunnel: performance, upgrades and new modes of operation," 2022.

[6] Glenn, A. B., Collen, P. L., and McGilvray, M., "Experimental Non-Equilibrium Radiation Measurements for Low-Earth Orbit Return," 2021.

[7] Steer, J., Collen, P. L., Glenn, A. B., Hambidge, C., Doherty, L. J., McGilvray, M., Loehle, S., and Walpot, L., "Shock Radiation Tests for Ice Giant Entry Probes Including CH4 in the T6 Free-Piston Driven Wind Tunnel," *AIAA SCITECH 2023 Forum*, 2023, p. 1729.

[8] Collen, P. L., Glenn, A. B., Doherty, L. J., and McGilvray, M., "Absolute Measurements of Air Shock-Layer Radiation in the T6 Aluminium Shock Tube," *Journal of Thermophysics and Heat Transfer*, 2023, pp. 1–14.

[9] Park, C., "Review of chemical-kinetic problems of future NASA missions. I-Earth entries," *Journal of Thermophysics and Heat transfer*, Vol. 7, No. 3, 1993, pp. 385–398.

[10] Brandis, A., Johnston, C., Cruden, B., Prabhu, D., and Bose, D., "Uncertainty analysis and validation of radiation measurements for earth reentry," *Journal of Thermophysics and Heat Transfer*, Vol. 29, No. 2, 2015, pp. 209–221.

[11] Brandis, A. M., Johnston, C. O., and Cruden, B. A., "Investigation of Non-Equilibrium Radiation for Earth Entry," 2016.

[12] Brandis, A., Johnston, C., Cruden, B., and Prabhu, D., "Equilibrium radiative heating from 9.5 to 15.5 km/s for earth atmospheric entry," *Journal of Thermophysics and Heat Transfer*, Vol. 31, No. 1, 2017, pp. 178–192.

[13] Cruden, B. A., and Brandis, A. M., "Measurement and prediction of radiative non-equilibrium for air shocks between 7-9 km/s," 2017.

[14] Gnoffo, P. A., Weilmuenster, K. J., Hamilton, H. H., Olynick, D. R., and Venkatapathy, E., "Computational aerothermodynamic design issues for hypersonic vehicles," *Journal of Spacecraft and Rockets*, Vol. 36, No. 1, 1999, pp. 21–43.

[15] Brandis, A. M., and Cruden, B. A., "Shock tube radiation measurements in nitrogen," *2018 Joint Thermophysics and Heat Transfer Conference*, 2018, p. 3437.

[16] Cruden, B. A., and Brandis, A. M., "Analysis of shockwave radiation data in nitrogen," *AIAA Aviation 2019 Forum*, 2019, p. 3359.

[17] Tibère-Inglesse, A. C., McGuire, S. D., Mariotto, P., and Laux, C. O., "Validation cases for recombining nitrogen and air plasmas," *Plasma Sources Science and Technology*, Vol. 27, No. 11, 2018, p. 115010.

[18] Kramida, A., Yu. Ralchenko, Reader, J., and and NIST ASD Team, NIST Atomic Spectra Database (ver. 5.11), [Online]. Available: `https://physics.nist.gov/asd` [2017, April 9]. National Institute of Standards and Technology, Gaithersburg, MD., 2023.

[19] Gildfind, D. E., James, C. M., Toniato, P., and Morgan, R. G., "Performance considerations for expansion tube operation with a shock-heated secondary driver," *Journal of Fluid Mechanics*, Vol. 777, 2015, pp. 364–407.

[20] Satchell, M., McGilvray, M., and Di Mare, L., "Analytical Method of Evaluating Nonuniformities in Shock Tube Flows: Theory and Development," *AIAA Journal*, 2021, pp. 1–15.

[21] Satchell, M., Glenn, A., Collen, P., Penty-Garaets, R., McGilvray, M., and di Mare, L., "An Analytical Method of Evaluating Nonuniformities in Shock Tube Flows. Part 2: Application," 2021.

[22] Collen, P. L., Satchell, M., di Mare, L., and McGilvray, M., "Analysis of Shock Deceleration Effects on Radiation Experiments in the NASA Electric Arc Shock Tube," *AIAA SCITECH 2022 Forum*, 2022, p. 0267.

[23] Clarke, J., Collen, P. L., McGilvray, M., and di Mare, L., "Numerical Simulation of a Shock Tube in Thermochemical Non-Equilibrium," *AIAA SCITECH 2023 Forum*, 2023, p. 1797.

[24] Mirels, H., "Test time in low-pressure shock tubes," *The physics of Fluids*, Vol. 6, No. 9, 1963, pp. 1201–1214.

[25] Mjolsness, R., and Ruppel, H. M., "Bremsstrahlung emission from low-energy electrons on atoms," *Physical Review*, Vol. 154, No. 1, 1967, p. 98.

[26] McBride, B. J., *Computer program for calculation of complex chemical equilibrium compositions and applications*, Vol. 2, NASA Lewis Research Center, 1996.

[27] Whiting, E. E., Park, C., Liu, Y., Arnold, J. O., and Paterson, J. A., "NEQAIR96, Nonequilibrium and Equilibrium Radiative Transport and Spectra Program: User's Manual," 1996.

[28] Cruden, B. A., and Brandis, A. M., "Updates to the NEQAIR radiation solver," *6th International Workshop on Radiation of High Temperature Gases in Atmospheric Entry*, 2014.

[29] Cruden, B., Martinez, R., Grinstead, J., and Olejniczak, J., "Simultaneous vacuum-ultraviolet through near-IR absolute radiation measurement with spatiotemporal resolution in an electric arc shock tube," *41st AIAA Thermophysics Conference*, 2009, p. 4240.

[30] Glenn, A., Collen, P., Jacobs, C., Laux, C., and McGilvray, M., "Comparison of Equilibrium Radiation Between Shock Tube and Plasma Torch Spectroscopy for Atmospheric Pressure Air," 2022.

[31] Clarke, J., Glenn, A. B., Di Mare, L., and McGilvray, M., "Numerical Simulations of Carbon Contaminants in T6 Shock Tube Tests," 2024.